Prenatal tuning of thalamic spontaneous activity patterns regulates somatosensory map resolution

Mar Aníbal-Martínez[1], Lorenzo Puche-Aroca[1], Gabriele Pumo[2,3], Dorien Vandael[1], M. Pilar Madrigal[4], Luis M. Rodríguez-Malmierca[1], Miguel Valdeolmillos[1], Francisco J. Martini[1], Filippo M. Rijli[2,3], Guillermina López-Bendito[1,*]

[1]Instituto de Neurociencias de Alicante, Universidad Miguel Hernández-Consejo Superior de Investigaciones Científicas (UMH-CSIC), San Juan de Alicante, Alicante, Spain.
[2] Friedrich Miescher Institute for Biomedical Research, Maulbeerstrasse 66, 4058 Basel, Switzerland.
[3]University of Basel, Basel, Switzerland.
[4]Departamento de Histología y Anatomía, Facultad de Medicina, Universidad Miguel Hernández (UMH), San Juan de Alicante, Alicante, Spain.

*Correspondence: g.lbendito@umh.es (G.L-B)

Keywords: sensory cortex, specification, barrel field, development, thalamus, calcium waves, whiskers, mouse

SUMMARY

Precise mapping of peripheral inputs onto cortical areas is required for appropriate sensory processing. In the mouse primary somatosensory cortex, mystacial whiskers are represented in large barrels, while upper lip whiskers are in smaller, less defined barrels. Traditionally, barrel size and definition are believed to be determined postnatally by whisker input and peripheral receptor density. However, prenatal thalamic spontaneous activity can influence somatosensory map development independently of whisker input. Thus, the mechanisms defining distinct barrel field territories, including size and definition, remain poorly understood. Here, we show that prenatal ablation of mystacial whiskers enhances the functional and anatomical definition of upper lip whisker barrels. These changes do not result from alterations in receptor density but rather stem from prenatal reconfigurations in the patterns of spontaneous activity within the thalamus. Our results unveil the role of prenatal synchronized thalamic activity in shaping cortical barrel size and functional map definition in the developing somatosensory system.

INTRODUCTION

Sensory systems are represented in the primary sensory areas of the brain, structured into both anatomical and functional maps[1-3]. The spatial precision of sensory maps varies among species according to the ethological relevance of the modality or the intra-modal sensory branch[4]. This precision is achieved through the accuracy of point-to-point innervation along the ascending sensory pathway. In rodents, which heavily rely on the somatosensory modality, a prominent cortical area is devoted to processing stimuli from facial whiskers. Within the mouse primary somatosensory cortex (S1), information from facial whiskers is processed in two juxtaposed subfields: the postero-medial barrel subfield (PMBSF) which receives input from the mystacial whiskers, providing diverse and specialized information to S1[5,6], and the antero-lateral barrel subfield (ALBSF), which receives input from the upper lip whiskers, considered to play a secondary role in sensory processing[7]. While each barrel corresponds to a single whisker in both regions, the degree of clustering of incoming thalamocortical axons varies, leading to notable anatomical distinctions between the two territories. While PMBSF barrels are characterized by their large size and sharp borders, ALBSF barrels are smaller and have apparently poorly defined borders[8]. These differences in intra-modal map organization parallel the distinct morphological characteristics of mystacial and upper lip whiskers: mystacial whiskers are long with large follicles, whereas upper lip whiskers are comparatively small, short, albeit more abundant. Yet, we still lack a complete understanding of the mechanism underlying the construction of these barrel maps and to what extent they rely on sensory receptors. Indeed, recent data demonstrated that sensory receptor-independent mechanisms can also influence cortical barrel size by altering the patterns of activity in subcortical stations. For instance, increasing thalamic waves in the developing somatosensory thalamus of early blind mice results in larger barrels in the PMBSF of S1, even before the onset of active whisking[9,10]. Thus, the size of a sensory barrel map may not only depend on the size and number of sensory receptors but may also be regulated by intrinsic programs during development. By embryonically ablating mystacial whiskers and follicles, and the subsequent PMBSF representation, we generated mice in which the ALBSF barrels become not only larger but better-defined, without altering the size and number of upper lip follicles. This intra-modal reorganization of the barrel map occurs within a restricted prenatal time window and is guided by modified patterns of spontaneous activity operating intra-modally in the thalamus. Interestingly, these modified ALBSF barrels resemble normal PMBSF barrels at the morphological, molecular and functional level, showing an enhanced spatial resolution upon tactile stimulation.

RESULTS

Barrel size and definition is determined prenatally independently of whisker type

Whisker map definition and barrel size are thought to be determined at early postnatal stages by the density of sensory receptors on the mouse face[11,12]. We asked whether prenatal removal of a selected facial whisker pattern might have an impact on cortical barrel size and spatial distribution of the spared whiskers. We implemented a strategy whereby the principal whiskers in the whisker pad were cauterized unilaterally at embryonic day (E) 14 (named as embWPC), in both wild type and TCA-GFP mice[13], in which thalamocortical projections are labeled with green fluorescent protein (GFP). At this stage, trigeminal nerve axons have just begun to target the principal trigeminal sensory nucleus (PrV) in the brainstem (**Figure S1A**), but PrV neuron axons have not yet entered the ventral posteromedial (VPM) thalamic nucleus[14-18] .

Analysis of the snout at E18 confirmed the specific ablation of the mystacial whiskers and follicles (**Figure 1A**), with a strong reduction of whisker pad-innervating primary trigeminal sensory axons targeting the principal nucleus (PrV) (**Figure S1B**). At early postnatal stages, the total areas of PrV, thalamic VPN (ventral-posterior nucleus), and S1 did not exhibit significant differences in embWPC, as compared to control mice (**Figures S2A-S2C**). In contrast, the size of the areas corresponding to mystacial and upper lip whiskers significantly rescaled in embWPC mice at all levels of the pathway, suggesting intra-modal plasticity of connectivity. For example, in S1, we found a 54% decrease in the PMBSF, and a 34% expansion of ALBSF, a phenomenon already observed at P4 (**Figures 1B** and **S2A-S2C**). Notably, we found no discernible differences in the total upper lip volume, nor in the volume and number of upper lip follicles between control and embWPC mice both at E18 and P8 (**Figures 1A** and **S2D**; **Videos S1** and **S2**). Dye depositions in the cortical PMBSF or ALBSF of P8 embWPC confirmed a similar intra-modal remapping of the corresponding PMBSF or ALBSF areas in the thalamic VPM[19] (**Figure S3A** and **S3B**); moreover, retrogradely labeled VPM neurons maintained a point-to-point distribution, matching cortical topography (**Figures S3C** and **S3D**).

Importantly, the changes of the cortical barrel field sub-territories depend on mechanisms only present before birth, since cauterization of the whisker pad at P0, referred to as P0WPC, revealed no significant territorial differences in the PMBSF and ALBSF between control and P0WPC across the somatosensory stations (**Figures 1C** and **S4**). As expected, there were no re-arrangements of the thalamocortical axons in the P0WPC (**Figure S5**). Thus, there is a critical window in which the cortical ALBSF area can be significantly adjusted without altering upper lip receptors, suggesting that

after this timepoint plasticity might arise from a different strategy to compensate for sensory loss.

Most interestingly, we observed that, beyond the overall increase in the cortical area occupied by the ALBSF, the average size of the cortical barrels was significantly increased in the ALBSF of the embWPC (**Figure 1D**). In addition to differences in barrel size, the PMBSF and the ALBSF differ in the extent of clustering of thalamocortical axons. Notably, the cortical map of the expanded ALBSF gained definition and contrast as thalamocortical terminals appear more clustered similarly to the control PMBSF (**Figure 1D**). Hence, our findings indicate the existence of an embryonic window for regulating the size and definition of cortical barrel maps (**Figure 1E**), a process that occurs independently of the type of peripheral receptors.

Functional remapping of ALBSF in embWPC mice occurs before birth and enhances topographical definition

Whisker pad stimulation *in vivo* at E18 can elicit activity in the developing PMBSF[20,21], indicating that the periphery-to-cortex somatosensory pathway is already functional before birth. We asked whether the anatomical changes observed in embWPC at P8 were detectable at earlier stages by assessing functional reorganizations. We carried out peripheral whisker pad and upper lip stimulations while recording cortical calcium activity in E18 *Emx1*^{GCaMP6f} transgenic mouse embryos, expressing GCaMP6f in cortical glutamatergic neurons[21] and carrying unilateral whisker pad cauterization (**Figure 2A**).

At E18, stimulations of either the whisker pad or the upper lip in the control side elicited responses from clusters of cortical neurons corresponding to the putative territories of the PMBSF or ALBSF, respectively (**Figure 2B**; **Video S3**). In contrast, whisker pad stimulations in the cauterized side (embWPC) triggered very reduced responses in the caudal-most part of the expected contralateral PMBSF ("PMBSF"), confirming the anatomical reduction of this territory. Remarkably, stimulations of the upper lip in the embWPC side elicited slightly misplaced responses within the expected ALBSF ("ALBSF") area that notably expanded into the "PMBSF" (**Figure 2B**; **Video S4**), as compared to the control side. This ectopic activation was maintained at P4 when the size of responses to upper lip stimulation were already refined in the control side (**Figures 2C-2E**; **Videos S5** and **S6**). Thus, the anatomical remapping of barrel field sub-territories seen in the postnatal embWPC can be functionally detected prior to birth.

We previously showed that, already before birth, PMBSF has a functional topographic organization correlating to the mystacial whisker spatial distribution of the snout[20]. In contrast, little is known about the functional topographical organization of ALBSF at E18. We asked whether the observed prenatal functional and spatial

reorganization of the ALBSF in embWPC might enhance the topographical definition of upper lip cortical barrel representation. To this aim, we carried out multi-point stimulations within the whisker pad or upper lip on both control and embWPC mice at E18 and P4 (**Figure 2F**). On the control mice at P4, cortical evoked responses confirmed a topographic organization of both PMBSF and ALBSF responses; however, while the PMBSF responses exhibited a well-defined and precise organization with virtually non-overlapping responses, those of the ALBSF were broader and less refined in comparison (**Figure 2G**; **Video S7**). Thus, beyond their anatomical idiosyncrasies, cortical barrel sub-fields also have a distinct degree of functional map definition as they emerge during perinatal development. This functional difference was not yet evident at E18 as functional responses from both the whisker pad and upper lip topographic stimulations greatly overlapped at this prenatal stage (**Figure 2G**; **Video S8**). Interestingly, stimulations at P4 from distinct skin locations of the upper lip of embWPC mice resulted in less overlapping responses within the ALBSF (**Figure 2G**; **Video S9**), a tendency already observed at E18 (**Video S10**). This suggests an enhanced spatial refinement giving rise to better topographic organization in the ALBSF of embWPC akin to that seen in the PMBSF map of control mice. In summary, these observations indicate that, in embWPC mice, a topographic functional remapping of the cortical ALBSF occurs before birth. This, in turn, results in enhancement of upper lip whisker topographic map resolution in early postnatal ALBSF.

Cortical ALBSF remapping correlates with thalamic ALBSF neurons adopting PMBSF-like transcriptomic signatures

Because thalamic input contributes to barrel formation[22], we asked whether the spatial and functional remapping of cortical barrel field sub-territories in embWPC embryos might correlate to transcriptional changes of thalamic input neurons. To assess this, we first dissected tissue from dorsolateral and ventromedial regions of the VPM of the thalamus, encompassing PMBSF and ALBSF, respectively, at P0 in control mice, and compared their transcriptional profiles by bulk RNA-sequencing (RNA-seq; **Figure S6A**). Principal component analysis (PCA) revealed that the transcriptomes from thalamic PMBSF and ALBSF cells in control mice clustered separately already at P0 (**Figure S6B**). Differential Expression Analysis (DEA) further revealed 377 Differentially Expressed Genes (DEGs) enriched in the thalamic PMBSF as opposed to 365 in the ALBSF cells (**Figures S6C** and **S6D**; **Table S1**). Among the DEGs enriched in each population, we found genes previously identified as being involved in somatosensory development such as *Rorβ*, *Slitrk6*, *Foxp2*, *Calb1* or *Lhx2*[9,23-26]. Remarkably, PCA analysis from thalamic ALBSF cells in embWPC mouse indicated that these neurons

grouped more closely with control PMBSF than ALBSF (**Figure 3A)**, with their transcriptional profile shifting toward a PMBSF pattern involving an expression change of 150 DEGs (**Figures 3B** and **3C**). Namely, in the ALBSF of the embWPC mouse, we observed an upregulation of approximately 17% of the DEGs normally expressed in the control PMBSF and a downregulation of about 23% of control ALBSF DEGs, respectively (**Figures 3D, S7A** and **S7B**; **Table S2**). Notably, genes such as *Rorα*, *Hs6st2*, *Cdh9*, or *Plxna2*, involved in axon guidance and PMBSF development[27], exhibited a PMBSF-like pattern in the ALBSF of embWPC mice (**Figures 3E, 3F** and **S7C**), also corroborated by in situ hybridization (**Figures S7D** and **S7E**). Next, we performed a Gene Ontology (GO) functional analysis of the genes with expression changes in the ALBSF of the embWPC and identified 11 clusters of GO-Terms enriched in Biological Processes (BP) and Molecular Functions (MF) (**Figures 3G**, **S7F** and **S7G**; **Table S3**). The top ranked cluster included 99 genes enriched in BP (46,76%) involved in dendrite development or synapse assembly (e.g. *Robo1, Flrt3*), and 12 genes enriched in MF (18,75%) involved in voltage-gated channel activity (e.g. *Kcnc2, Kcnab1*). In summary, the spatial remapping and functional enhancement of cortical ALBSF map definition in embWPC correlate to transcriptomic changes observed in ALBSF thalamic input neurons, which shift towards a molecular signature resembling that of PMBSF neurons.

Increasing prenatal spontaneous activity in thalamic sub-territories enhances ALBSF spatial definition

The aforementioned results indicate that the molecular identity of the thalamic ALBSF in embWPC mice resembles that of the wild type PMBSF. One of the most prominent transcriptional alterations involves changes in the expression of genes associated with neuronal activity. Hence, we wondered whether ALBSF neurons in embWPC might acquire PMBSF-like activity patterns.

Thalamic neurons display waves of prenatal spontaneous activity that are crucial for the development of cortical barrel field maps[9,20]. Therefore, we investigated whether the lack of whisker pad input in embWPC embryos could lead to changes in spontaneous activity patterns in VPM neurons. Inputs from the whisker pad at E16 are carried by afferents from ventral portion of the PrV (vPrV), whereas inputs from the upper lip are carried by afferents from dorsal PrV (dPrV)[16-18]. While vPrV afferents topographically target the PMBSF primordium in dorsolateral VPM (VPMlat), prenatal dPrV afferents target not only the ventromedial part (VPMmed, ALBSF primordium) but cover most part of the VPM[16,18]. Thus, while whisker pad and upper lip inputs are segregated at the brainstem nuclei, dPrV and vPrV axons terminals prenatally overlap within the prospective PMBSF territory[16,18] (**Figure 4A** and **S8**). Remarkably, despite this axonal

overlap, spontaneous activity patterns at E16 (**Figure 4B**) were sub-territory specific. We detected a notable distinction in the spontaneous activity waves patterns between VPMlat and VPMmed regions. While VPMlat exhibited a high frequency of waves, VPMmed showed significantly reduced frequency (**Figure 4C**; **Video S11**).

In embWPC, we observed a significant change in the spontaneous activity patterns compared to control mice, with a striking increase in thalamic waves frequency within the VPMmed, resembling the pattern observed in the VPMlat (**Figure 4B** and **4C**; **Video S12**). Thus, during prenatal development whisker input deprivation functionally remaps spontaneous neuronal activity patterns in the future ALBSF, acquiring a similar activity frequency as normally shown by PMBSF neurons. The increased activity in the VPMmed correlated with the enlarged and more defined ALBSF barrels, akin to the PMBSF, observed in the postnatal cortex of embWPC mice (**Figure 1D**).

Next, we hypothesized that during prenatal development distinct frequencies of thalamic spontaneous activity waves in dorsolateral and ventromedial VPM might contribute to regulate postnatal distinct barrel size and map definition in cortical PMBSF and ALBSF. To test this, we first analyzed the impact of disrupting the normal pattern of spontaneous thalamic activity on the map size and definition in the barrel field cortical areas by crossing a tamoxifen-dependent *Gbx2*^{CreERT2} mouse with a floxed line expressing the inward rectifier potassium channel 2.1 (*Kcnj2*) fused to the mCherry reporter (referred to as *Th*^{Kir})[20]. Anatomical analysis of the thalamic and cortical PMBSF and ALBSF showed a relatively minor but significant decrease in the size of the PMBSF areas (around 17% in the thalamus and 13% in the cortex, respectively) and an about 20% increase in the size of the ALBSF thalamic area (**Figures 4D, S9A** and **S9B**). Nevertheless, and as previously described[20], the most apparent change in the *Th*^{Kir} mouse was the complete loss in barrel definition, evidenced by a total lack of TCA clustering, in both PMBSF and ALBSF that could be also functionally identified by a higher overlap in the responses to both whisker pad and upper lip stimulation experiments at P4 (**Figure 4E**; **Videos S13** and **S14**). We then reasoned that if thalamic activity is crucial to confer barrel size and map definition, irrespective of territory size, then silencing thalamic activity in embWPC should not impact or prevent intra-modal thalamic and cortical remapping, but the gain in ALBSF barrel size and map definition would be impaired. To test this, we conducted embryonic whisker pad cauterization in *Th*^{Kir} (referred to as embWPC-*Th*^{Kir}) and assessed the postnatal segregation and definition of barrel-field maps. Our data revealed that thalamic and cortical territories in embWPC-*Th*^{Kir} mice exhibited a territorial reorganization similar to that observed in embWPC mice. In both cases, the PMBSF virtually disappeared, and the ALBSF expanded as compared to the control (**Figure 4F**). Yet, manipulating thalamic activity

patterns resulted in a complete inability to achieve barrel definition in the expanded ALBSF area in the embWPC-*Th*^{Kir} mouse (**Figure 4F**). In sum, our results demonstrate that the spatial resolution of cortical somatosensory maps relies on specific patterns of spontaneous activity in the distinct thalamic sub-territories during prenatal development (**Figure 4G**).

DISCUSSION

Our study underscores the role of thalamic spontaneous activity patterns in shaping the size and definition of somatosensory cortical representations. We demonstrated that the thalamic PMBSF region, responsible for processing input from mystacial whiskers, displays a distinct pattern of spontaneous activity and transcriptional signature, as compared to the ALBSF. Both activity-driven and genetic factors contribute to the remarkable anatomical and functional topographical accuracy observed in this region during development. Furthermore, our findings suggest that a similar mechanism may be engaged during embryonic stages to reconfigure sensory circuits, especially under deprived conditions, thereby enhancing spatial discrimination in regions such as the ALBSF where cortical representations are otherwise less defined.

The developmental relationship between sensory receptors and somatosensory representations has been thoroughly examined in prior work involving mice and rats. Deprivation of a single whisker or a row of whiskers during the first postnatal week, leads to the loss of the corresponding cortical barrels and enlargement of the surrounding barrels [28-33]. Furthermore, rewiring of ipsilateral trigeminal input from mystacial whiskers to the ipsilateral barrel field generates an ectopic barrel field within the normal barrel map[34]. Collectively, these studies highlight the sensitivity of barrel maps to manipulations in peripheral or sensory input. Additionally, research has established a correlation between the size of cortical barrels and the size of corresponding sensory receptors, resulting in large barrels in the PMBSF corresponding to long mystacial whiskers[11,12]. These whiskers, also known as macrovibrissae, hold significant behavioral relevance for the animal, being the first ones used for search of objects and gaps, and to discern diverse tactile features such as object's position, shape or texture[35].

ALBSF barrels, corresponding to short whiskers from the upper lip snout, are comparatively smaller, less defined and densely packed than those in the PMBSF[8,36,37]. Although the function of these shorter whiskers, also known as microvibrissae, remains largely unexplored, they appear to primarily aid in object discrimination when the snout is in close proximity to the object[7,38-40]. Given their anatomical and functional disparities, the PMBSF and ALBSF represent two distinct somatosensory subsystems. Consequently, we initially expected minimal reorganization of the ALBSF upon

deprivation of the whiskers corresponding to the PMBSF. However, our data from mice deprived of mystacial whiskers at embryonic stages (embWPC mice) reveal a notable switch in the developmental program of the ALBSF, leading to the formation of large and well-defined barrels. These findings highlight a decoupling of mechanisms governing the type, size, and density of sensory receptors from those influencing the size and definition of cortical representations. Specifically, we observed that the immature brain possesses mechanisms to develop a barrel field with anatomical and functional characteristics akin to the PMBSF, regardless of the type of peripheral receptor. Therefore, our findings indicate that the brain may construct a barrel map capable of processing more intricate tactile functions for the animal, even in scenarios involving small receptors with subsidiary functions.

Using embWPC mice, we demonstrated that the enlargement of cortical ALBSF barrel size and definition is guided by the thalamus. This reorganization capability is temporally constrained during prenatal development, anticipating the closure of the critical time window for somatosensory circuits[30,41]. In this mouse model, the transcriptional profile of the thalamic region innervating the ALBSF mirrors that of the PMBSF in control mice. Crucial genes for thalamocortical barrel field development, such as *Ror*α or *Epha4*[27,42], altered their expression pattern in the expanded region of the thalamus innervating the ALBSF. For instance, we observed an upregulation of *Ror*α in this region, suggesting a potential role in increasing the density and clustering of axonal terminals in layer 4. This hypothesis is supported by a previous study demonstrating that conditional deletion of *Ror*α in thalamic neurons results in complete loss of cortical PMBSF barrels[27]. Additionally, we identified alterations in genes associated with neuronal activity, including ion channels, which may contribute to or reflect the modified pattern of thalamic activity observed in the embWPC model. Consequently, activity-dependent gene regulation could also operate in the reorganization of the thalamocortical ALBSF pathway, as axon growth and genesis are activity-dependent processes during thalamic development[43,44].

Remarkably, our findings indicate that the determinants of cortical area size operate independently of overall neuronal activity, whereas achieving barrel size and spatial discrimination relies on thalamic activity patterns. Thalamic spontaneous activity is key for the emergence of cortical somatosensory maps, as evidenced by the fact that suppressing this activity leads to mice that do not develop barrels despite having normal whiskers[20]. Indeed, we observed that Th^{Kir} mice failed to develop a precise functional topography in any of the barrel sub-fields. Our study indicates that the mechanisms responsible for the expansion of ALBSF still occur in the embWPC-Th^{Kir} mice, which lack synchronous thalamic activity. However, this enlargement was not accompanied by the

increase in barrel size and definition found in the ALBSF of embWPC mice. Thus, our study unveils a novel role for this early patterned thalamic spontaneous activity in fine-tuning barrel definition across sensory maps. The differences in frequency and pattern of thalamic waves between VPM sub-fields may serve as a mechanism to facilitate the development of distinct cortical representations specialized in processing specific features of touch.

Author contributions

Conceptualization, M.A-M. and G.L-B.; methodology, M.A-M., G.P., D.V., MP.M. and LM R-M.; data curation, M.A-M., G.P., D.V., and L.P.; transcriptomic analysis, L.P.; writing – original draft, M.A-M., and G.L-B.; writing – review & editing, M.A-M., L.P., G.P., D.V., M.V., FJ.M., FM.R., and G.L-B.; funding acquisition, FM.R., and G.L-B.; resources, FM.R., and G.L-B.; supervision, M.V., FJ.M., FM.R., and G.L-B.

Acknowledgements

We thank Belén Andrés and María Aurelia Torregrosa for their technical support. We thank Teresa Guillamón-Vivancos for her comments on the manuscript and other members of López-Bendito's laboratory for stimulating discussions. D.V. was supported by FJC2021-046529-I funded by MCIN/AEI/10.13039/501100011033 and by the European Union NextGenerationEU/PRTR. This work was supported by grants from the Swiss National Science Foundation (31003A_175776 and 310030_219370) and the Novartis Research Foundation to F.M.R., and by grants from the European Research Council (ERC) under the European Union's Horizon 2020 research and innovation programme (ERC-2021-ADG-101054313 SPONTSENSE), PID2021-127112NB-I00 from the MCIN/AEI /10.13039/501100011033/ and ERDF A way to make Europe, and Generalitat Valenciana, Conselleria d'Educació, Universitats, i Ocupació (PROMETEO 2021/052) to G.L.-B.

Declaration of interest

The authors declare no competing interests.

Main Figures

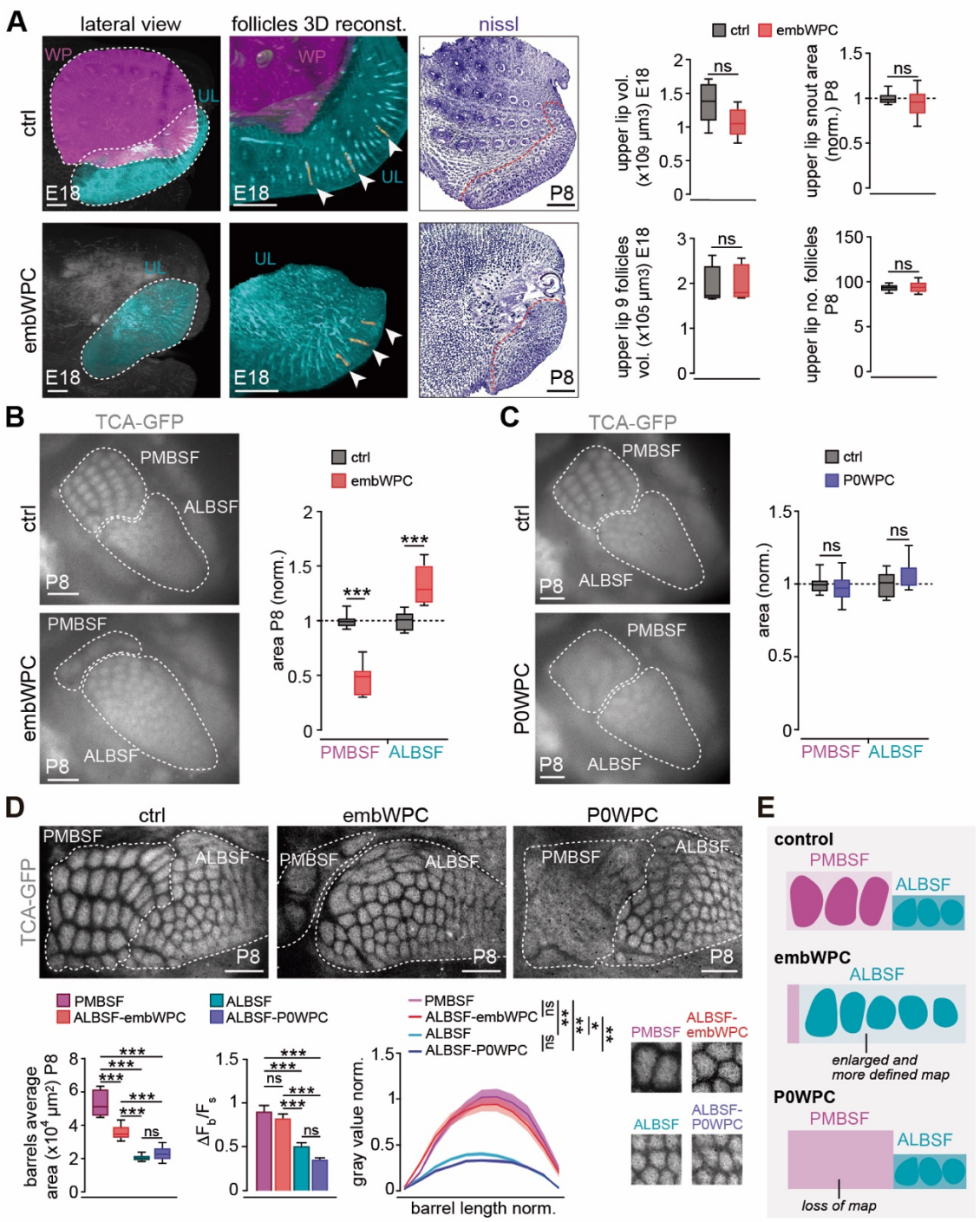

Figure 1. Whisker pad deprivation in embryos enhances definition of upper lip barrel field territory. (A) Left and middle, iDISCO lateral views of whisker pad (magenta) and upper lip (cyan), and 3D-reconstructions of the follicles (yellow) of the snout at E18 in control and after whisker pad cauterization of the mystacial whiskers mice. Right, Nissl stainings of the snout at P8 in control and embWPC mice, red dashed line delimits upper lip area. Quantification of the data (iDISCO E18, n= 5 ctrl mice, n= 5 embWPC mice, upper lip volume, unpaired two-tailed Student *t*-test. ns, p= 0.11; upper lip 9 follicles volume, Mann-Whitney *U*-test. ns, p= 0.73. Nissl P8, n= 8 ctrl mice, n= 9 embWPC mice, upper lip area, unpaired two-tailed Student *t*-test. ns, p= 0.32; upper lip number of follicles, unpaired two-tailed Student *t*-test. ns, p= 0.78). **(B)** Surface view of thalamocortical terminals (TCA-GFP+) in the cortical

PMBSF and ALBSF in control and embWPC mice at P8. Quantification of the data (n= 8 ctrl mice, n= 9 embWPC mice, unpaired two-tailed Student *t*-test). **(C)** Surface view of thalamocortical terminals (TCA-GFP+) in the cortical PMBSF and ALBSF in control and P0WPC mice at P8. Quantification of the data (n= 8 ctrl mice, n= 9 P0PC mice, unpaired two-tailed Student *t*-test. ns, PMBSF, p= 0.55, ALBSF, p= 0.30). **(D)** Top, cortical flattened tangential sections showing thalamocortical terminals (TCA-GFP+) in the PMBSF and ALBSF in control, embWPC and P0WPC mice at P8. Bottom right, insets show in detail the clustering of TCA in each condition. Quantification of the data (Barrel average area of 34 barrels, n= 7 ctrl mice PMBSF, n= 9 ctrl mice ALBSF, n= 9 embWPC mice ALBSF, n= 5 P0WPC mice ALBSF, Two-way ANOVA test: ***p <0.001. Tukey's multiple comparison test post-hoc analysis, ns, p= 0.88; ΔFb/Fs: barrel/septum fluorescence ratio, n= 12 ctrl mice PMBSF, n= 13 ctrl mice ALBSF, n= 13 embWPC mice ALBSF, n= 5 P0WPC mice ALBSF, Two-way ANOVA test: ***p <0.001. Tukey's multiple comparison test post-hoc analysis, PMBSF-ctrl vs ALBSF-embWPC ns, p= 0.80; ALBSF-ctrl vs ALBSF-P0WPC ns, p= 0.35; Gray value, n= 66 ctrl PMBSF barrels, n= 65 ctrl ALBSF barrels, n= 42 embWPC ALBSF barrels, n= 25 P0WPC ALBSF barrels, One-way ANOVA test: ***p <0.001. Tukey's multiple comparison test post-hoc analysis, ns, p= 0.99). **(E)** Schema illustrating the results found. WP, whisker pad; UL, upper lip; E, embryonic; P, postnatal; embWPC, embryonic whisker pad cauterized; P0WPC, postnatal day 0 whisker pad cauterized; vol., volume; no., number; TCA-GFP, thalamocortical axons labelled with green fluorescent protein; PMBSF, postero-medial barrel subfield; ALBSF, antero-lateral barrel subfield; norm., normalized. Scale bars, (A) (left) 300 μm; (A) (middle) 400 μm; (A) (right) 1000 μm; (B), (C) and (D) 500 μm. Boxplots show the medians with the interquartile range (box) and range (whiskers). Bar graphs show the means ± SEM. ns, not significant. *p < 0.05, **p < 0.01 ***p < 0.001. See also Figures S1-S5; Videos S1 and S2.

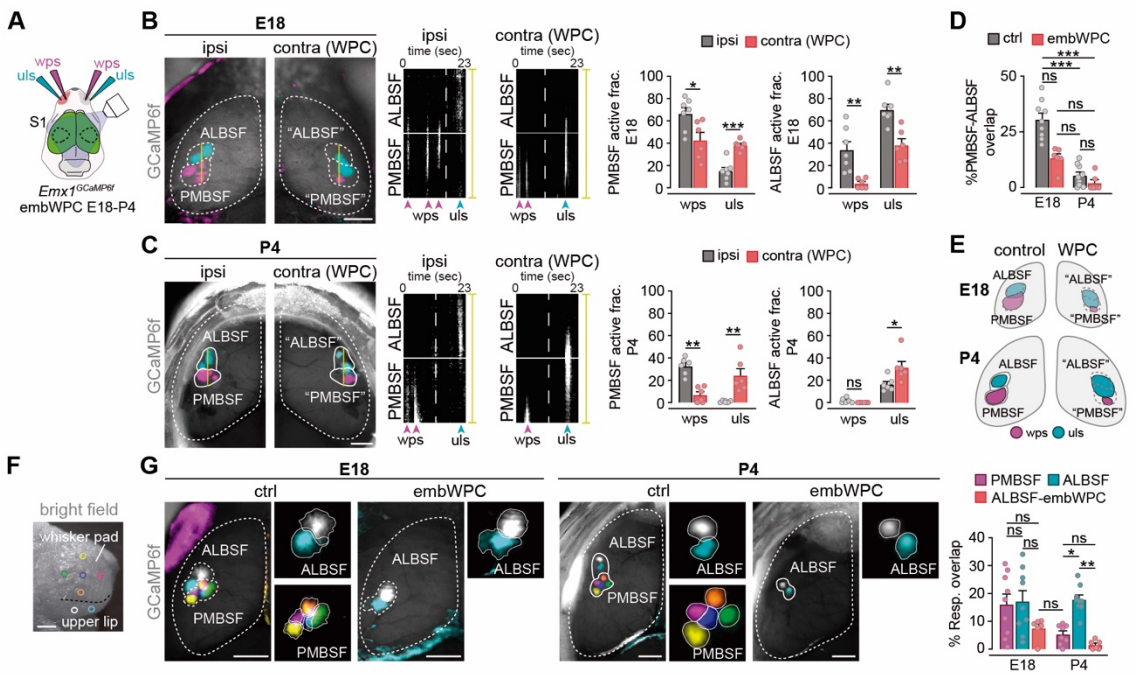

Figure 2. Functional reorganization of cortical barrel field territories in response to embryonic whisker pad deprivation. (A) Schema representing the experimental paradigm. **(B)** Left, cortical evoked responses (GCaMP6f) to whisker pad (magenta) and upper lip (cyan) stimulations in control (ipsilateral) and whisker pad cauterized (WPC, contralateral) sides in embWPC mice at E18. Control PMBSF and ALBSF territories were translated to the WPC side for direct comparison and labelled as "PMBSF" and "ALBSF". Right, reslice of the yellow line in the left, representing responses elicited in PMBSF and ALBSF primordia by whisker pad stimulation (wps) or upper lip stimulations (uls). The white horizontal line delineates the boundaries between PMBSF and ALBSF, while the vertical dashed line divides the wps from the uls over time. Quantification of the PMBSF and ALBSF active fraction to wps or uls (n= 7 ctrl, n= 6 WPC, unpaired two-tailed Student *t*-test). **(C)** Left, cortical evoked responses (GCaMP6f) to whisker pad (magenta) and upper lip (cyan) stimulations in control (ipsilateral) and WPC (contralateral) sides in embWPC at P4. Right, reslice of the yellow line in the left, representing responses elicited in PMBSF or ALBSF by wps or uls. The white horizontal line delineates the boundaries between PMBSF and ALBSF, while the vertical dashed line divides the wps from the uls over time. Quantification of the PMBSF and ALBSF active fraction to wps and uls (n= 6 ctrl side, n= 6 WPC side, PMBSF active fraction, unpaired two-tailed Student *t*-test; ALBSF active fraction, Mann-Whitney *U*-test. ns, p= 0.06). **(D)** Quantification of the percentage of overlap responses between the PMBSF and ALBSF territories at E18 and P4 (n= 9 ctrl mice E18, n= 6 embWPC mice E18, n= 9 ctrl mice P4, n= 6 embWPC mice P4, Kruskal-Wallis test, ***p <0.001. Dunn's multiple comparison test post-hoc analysis, ctrl E18 vs embwpc E18 ns, p= 0.37; embWPC E18 vs ctrl P4 ns, p= 0.77; embWPC E18 vs embWPC P4 ns, p= 0.14; ctrl P4 vs embWPC P4 ns, p > 0.99). **(E)** Schema illustrating the results found. **(F)** Schema representing the experimental paradigm. **(G)** Cortical evoked responses (GCaMP6f) to five distinct whisker pad stimulations and two distinct upper lip stimulations in control and embWPC mice at E18 and P4. Dashed lines indicate the territory covered by elicited responses within the PMBSF and ALBSF. Quantification of the percentage of overlap between two distinct PMBSF and two distinct ALBSF responses at E18 and P4 (n= 9 ctrl mice E18 for PMBSF and ALBSF responses, n= 6 embWPC mice E18 for ALBSF responses, n= 8 ctrl mice P4 for PMBSF responses, n= 9 ctrl mice P4 for ALBSF responses, n= 6 embWPC mice P4 for ALBSF responses, Kruskal-

Wallis test, ***p <0.001. Dunn's multiple comparison test post-hoc analysis, ns, p >0.99). Dashed lines delineate PMBSF and ALBSF putative evoked territories at E18. S1, primary somatosensory cortex; wps, whisker pad stimulation; uls, upper lip stimulation; GCaMP6f, calmodulin-based genetically encoded fluorescent calcium indicator 6–fast; WPC, whisker pad cauterized; contra, contralateral cortex to the whisker pad cauterized; ipsi, ipsilateral cortex to the whisker pad cauterized. Scale bars, 1000 μm. Bar graphs show the means ± SEM. ns, not significant. *p < 0.05, **p < 0.01 ∗∗∗p < 0.001. See also Figures S1-S3; Videos S3-S10.

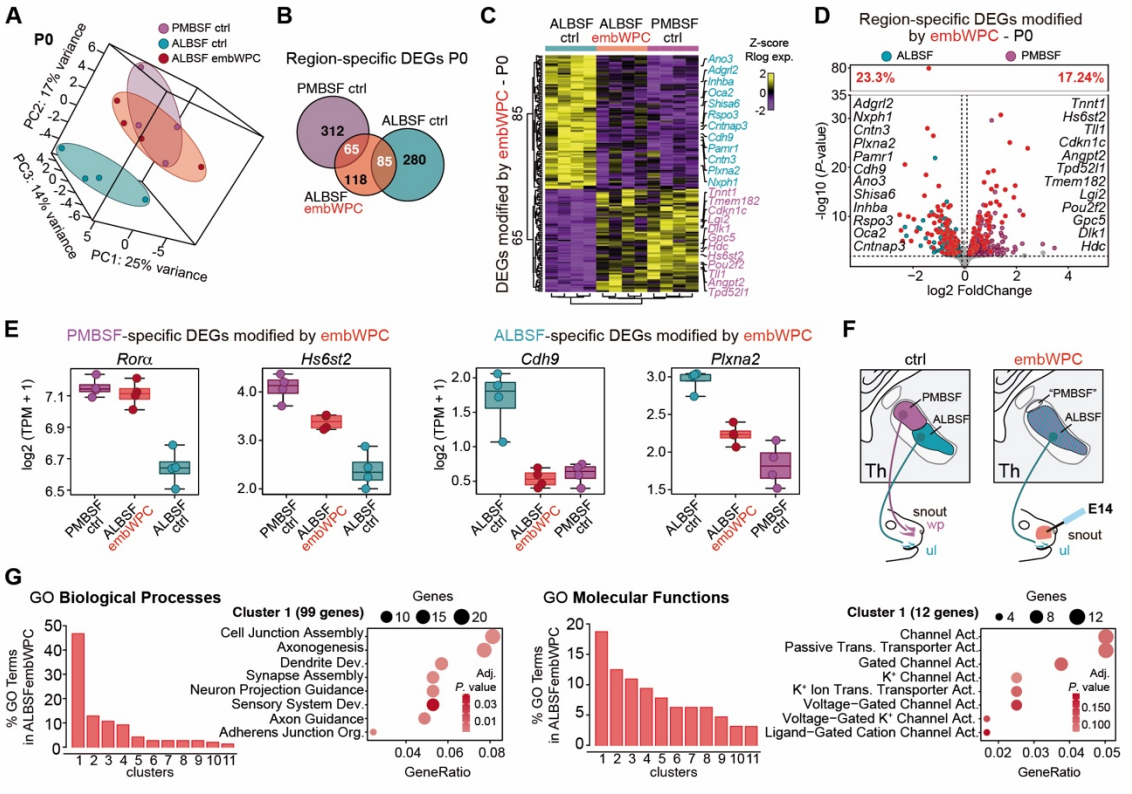

Figure 3. Thalamic ALBSF incorporates transcriptional signatures from PMBSF. (A) Principal Component Analysis (PCA) of PMBSF control (n= 4), ALBSF control (n= 4) and ALBSF whisker pad cauterization (embWPC, n= 4) at P0. **(B)** Venn Diagram shows the number of genes modified by embWPC in ALBSF overlapped in every subset of region specific Differentially Expressed Genes (DEGs). **(C)** Heatmap of the normalized regularized logarithm (Rlog) Z-score of expression and unbiased clustering of region-specific DEGs whose expression was modified by embWPC in the ALBSF at P0. **(D)** Volcano plot showing the significance and *P*-value distribution of DEGs. The magenta and cyan dots represent PMBSF and ALBSF DEGs, respectively, while the red dots and the percentages represent area specific DEGs shifted by embWPC with the top 12 protein coding genes listed in every region. **(E)** Boxplots showing TPM expression levels of selected PMBSF-specific and ALBSF-specific DEGs modified by embWPC in the ALBSF. Boxplots show the medians with the interquartile range (box) and range (whiskers). **(F)** Schema illustrating the results found. **(G)** Gene Ontology (GO) functional analysis (Biological Processes, left; and Molecular Functions, right) showing the top ranked clusters of GO terms enriched in the region-specific gene-set modified in embWPC-ALBSF. See also Figures S6-S7.

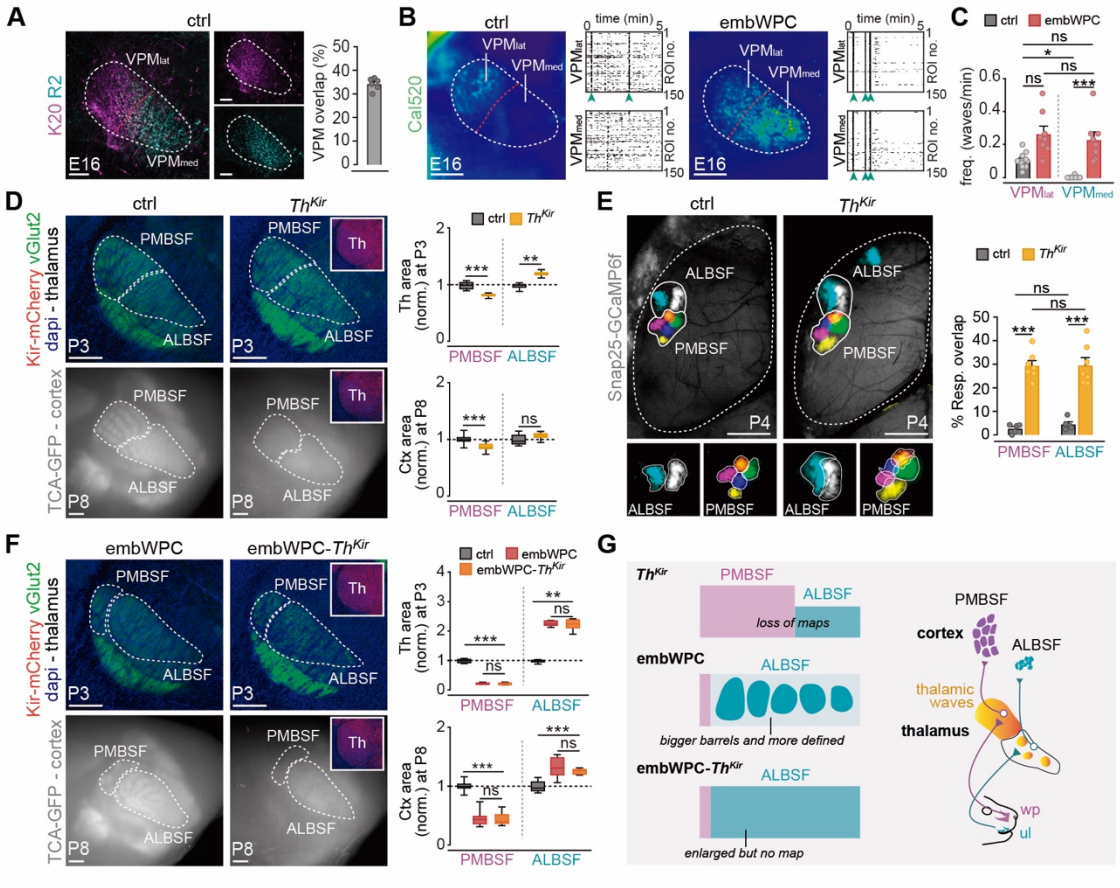

Figure 4. Improved upper lip barrel field map discrimination relies on thalamic patterned activity. (A) Coronal sections from the *Krox20-zsgreen::R2-mCherry* double transgenic mouse showing Krox20-labelled axons (magenta, vPrV) and R2-labelled axons (cyan, dPrV) at the VPM of the thalamus at E16. Quantification of the percentage of overlap of labelled axons at the thalamus (n= 6). **(B)** Spontaneous calcium activity in the VPM regions (VPMlat, dorsolateral; and VPMmed, ventromedial) of the thalamus in acute slices at E16. Raster plots of 5 minutes. **(C)** Quantification of the frequency of waves activity in the VPM in both control and embWPC mice (n= 11 ctrl mice, n= 8 embWPC mice, Kruskal-Wallis test, ***p <0.001. Dunn's multiple comparison test post-hoc analysis, ctrl VPMlat vs embWPC VPMlat ns, p= 0.14; ctrl VPMlat vs embWPC VPMmed ns, p= 0.32; embWPC VPMlat vs embWPC VPMmed ns, p >0.99). **(D)** Upper panels, coronal sections of vGlut2 staining (green) showing the size of PMBSF and ALBSF territories in the thalamus of control and *Th*^{Kir} mouse (Kir-mCherry positive) at P3. Lower panels, surface view of thalamocortical terminals (TCA-GFP+) in the cortical PMBSF and ALBSF in control and *Th*^{Kir} mice at P8. Quantification of the data (Thalamus, n= 5 ctrl mice, n= 6 *Th*^{Kir} mice, PMBSF, unpaired two-tailed Student *t*-test; ALBSF, Mann-Whitney *U*-test. Cortex, n= 10 ctrl mice, n= 10 *Th*^{Kir} mice, unpaired two-tailed Student *t*-test. ns, p= 0.99). **(E)** Cortical evoked responses (GCaMP6f) to five distinct whisker pad and two distinct upper lip stimulations in control and *Th*^{Kir} mice at P4. Quantification of the percentage of overlap between two distinct PMBSF and two distinct ALBSF responses (n= 5 ctrl mice, n=7 *Th*^{Kir} mice, Two-way ANOVA test: ***p <0.001. Tukey's multiple comparison test post-hoc analysis, ns, p> 0.96). **(F)** Upper panels, coronal sections of vGlut2 staining (green) showing the size of PMBSF and ALBSF territories in the thalamus of embWPC and embWPC-*Th*^{Kir} mouse (Kir-mCherry positive) at P3. Lower panels, surface view of thalamocortical terminals (TCA-GFP+) in the cortical PMBSF and ALBSF in embWPC and embWPC-*Th*^{Kir} mice at P8. Quantification of the data (Thalamus, n= 5 ctrl mice, n= 5 embWPC mice, n= 6 embWPC-*Th*^{Kir} mice, PMBSF, Two-way ANOVA test: ***p <0.001. Tukey's multiple comparison test post-hoc analysis, ns, p= 0.98; ALBSF, Kruskal-Wallis test, ***p <0.01. Dunn's multiple comparison test post-hoc analysis, ns, p >0.99. Cortex, n= 10 ctrl mice, n= 13 embWPC mice, n= 7 embWPC-*Th*^{Kir} mice, PMBSF, Two-way ANOVA test: ***p

<0.001. Tukey's multiple comparison test post-hoc analysis, ns, p= 0.99; ALBSF, Two-way ANOVA test: ***p <0.001. Tukey's multiple comparison test post-hoc analysis, ns, p= 0.52). **(G)** Schema illustrating the results found. Cal520, calcium indicator 520; Th, thalamus; Th^{Kir}, thalamic Kir2.1 expression mice. Scale bars, (A) 100 μm; (C) 200 μm; (D) (top) and (F) (top) 250 μm, (D) (bottom) and (F) (bottom) 500 μm; (E) 1000 μm. Boxplots show the medians with the interquartile range (box) and range (whiskers). Bar graphs show the means ± SEM. ns, not significant. *p < 0.05, **p < 0.01 ∗∗∗p < 0.001. See also Figures S8-S9; Videos S11-S14.

STAR Methods text

Declaration of generative AI and AI-assisted technologies in the writing process

During the preparation of this work the authors used Chat-GPT in order to streamline some parts of the text. After using this tool, the authors reviewed and edited the content as needed and take full responsibility for the content of the publication.

Resource Availability

Lead contact

Additional information and requests for resources and reagents should be directed to the lead contact, Guillermina López-Bendito (g.lbendito@umh.es).

Materials availability

This study did not generate new mouse lines.

This study did not generate new unique reagents.

Data and code availability

This study did not generate original code. For *ex vivo* experiments analysis, calcium imaging code previously reported[20] has been deposited at https://github.com/ackman678/CalciumDX. For *in vivo* calcium imaging experiments, the code from WholeBrainDX repository[45] (available at https://github.com/ackman678/wholeBrainDX) was employed to prepared the supplementary videos.

RNAseq datasets have been deposited at the National Center for Biotechnology Information (NCBI) Gene Expression Omnibus (GEO) and are publicly available as of the date of publication. Accessions numbers are listed in the key resources table.

Any additional information required to reanalyze the data reported in this work paper is available from the lead contact upon request.

Experimental model and study participant details

Animals

All animal experiments were conducted in accordance with the ARRIVE guidelines and conformed to the Committee on Animal Research at the University Miguel Hernández that approved all the animal procedures, which were carried out in compliance with Spanish and European Union regulations. Similar numbers of male and female mice were used interchangeably. No sex-related differences were observed in the measurements throughout the study. Mice were maintained in pathogen-free facilities under standard housing conditions with continuous access to food and water on a 12h light-dark cycle. The number of animals used in each experiment is noted in the figure legends.

All mouse transgenic lines in this study were maintained on an ICR/CD-1 genetic background and genotyped by PCR. The *TCA-GFP Tg*, in which the TCAs are labelled with GFP, the *R26*$^{Kir2.1\text{-}mCherry}$, mouse lines were previously described[13,9,20]. The Cre-dependent mouse line, *R26*^{GCaMP6f} was obtained from Jackson Laboratories (Stock number 024105) and crossed with an *Emx1*$^{Cre/+}$ transgenic mouse[46] to conditionally express the fast calcium indicator GCaMP6f in glutamatergic cortical neurons (*Emx1*^{GCaMP6f})[20,21]. The *R26*$^{Kir2.1\text{-}mCherry}$ mice were crossed with an inducible *Cre*^{ERT2} mouse line driven by *Gbx2*, an early specific thalamic promoter (*Gbx2*$^{CreERT2/+}$)[47]. Double mutants are referred as *Th*^{Kir} and triple mutants as *TCA-GFP-Th*^{Kir} [20]. The *r2*^{mCherry}[18], *Krox20*^{Cre}[48] and *R26RZsGreen* (Jackson Laboratories, Stock number 007906)[49] lines, were as described. We crossed *Krox20*^{Cre} with *R26RZsGreen* to generate double mutants *Krox20*^{ZsGreen} and we also generated *Krox20*^{ZsGreen}*::r2*^{mCherry} triple mutants. The *Snap25-GCaMP6f* mouse line (Jackson Laboratories, 025111) expresses GCaMP6f slow variant of calcium indicator[49]. This mouse line was crossed with *Th*^{Kir} to conditionally express the GCaMP6f in excitatory neurons. Tamoxifen induction of Cre recombinase in the double/triple mutant embryos was performed by gavage administration of tamoxifen (5 mg dissolved in corn oil, Sigma) at E10 to specifically target all primary sensory

thalamic nuclei. Tamoxifen administration in pregnant mice produces non-desirable side effects such as delivery problems and decrease survival of newborn pups[50]. To increase the survival rate of young pups, we administered 125 mg/Kg of progesterone (DEPO-PROGEVERA®) intraperitoneally at E14 and implemented C-section procedure at E19. Pups were then placed with a foster mother. In all cases, the Cre^{ERT2}-negative littermates were used as controls of the experimental condition.

Method details

Histology

For *in situ* hybridization and immunohistochemistry at postnatal stages, mice were perfused with 4% paraformaldehyde (PFA) in PBS (0.01 M), and their brains were subsequently removed and post-fixed in the same fixative overnight. For immunohistochemistry of embryonic tissue, the brains were dissected out and immediately fixed in 4% PFA overnight. For Nissl staining, a microtome (MICROM) was used to cut paraffin slices of 5 μm. Next, the sections were stained in 0.5% cresyl violet (Sigma) solution for 15-25 min and then rinsed quickly in distilled water. After decolorization in 70% ethyl alcohol for few seconds, the sections were dehydrated in 95%, 100% ethyl alcohol for 2 to 3 min, cleared in xylen (Sigma) for 2 min and mounted with Eukitt (Merk). Cytochrome oxidase staining was performed to label the PrV territories. For cytochrome Oxidase (CytOx) staining, 80 μm vibratome coronal sections were incubated overnight at 37 ºC in a CytOx solution: 0.03% cytochrome c (Sigma C2506), 0.05% 3-3′ diaminobenzidine tetrahydrochloride hydrate (DAB, Sigma D5637) and 4% sucrose in PBS. For tangential sections, cortical hemispheres were flattened and cryoprotected through steps of 10%, 20% and 30% of sucrose in PBS. Then, a cryotome (MICROM) was used to cut at 80 μm tangential sections. Immunohistochemistry was performed on 80 μm vibratome or cryotome brain sections (coronal and tangential), which were first incubated for 1h at room temperature in a

blocking solution containing 1% BSA (Sigma) and 0.25% Triton X-100 (Sigma) in PBS. Afterwards, the slices were incubated overnight at 4 °C with the following primary antibodies: guinea pig anti-vGlut2 (1:10000, Synaptic Systems, 135404), chicken anti-GFP (1:3000; Aves Labs, GFP-1020), rat anti-RFP (1:1000 Chromotek, 5F8) and rabbit anti-RFP (1:1000, Rockland, 600-401-379). Sections were then rinsed in PBS and incubated for 2h at room temperature with secondary antibodies: Alexa488 donkey anti-guinea pig (1:500, ThermoFisher, A11073), Alexa488 goat anti-chicken (1:500, ThermoFisher, A11039), Alexa594 donkey anti-rat (1:500, ThermoFisher, A21209) and Alexa goat 568 anti-rabbit (1:500, Invitrogen, A11011). Counterstaining was performed using the fluorescent nuclear dye 4′,6-diamidino-2-phenylindole (DAPI) (Sigma). In situ hybridization was performed on 60 μm vibratome sections using digoxigenin-labelled antisense probe for *Ror*α, *Pou2f2*, *Hs6st2*, *Plxna2* and *Cdh9*. Hybridization was carried out overnight at 65 ºC, and after hybridization, the sections were washed and incubated overnight at 4 ºC with an alkaline phosphatase-conjugated anti-digoxigenin antibody (1:2500-1:4000, Roche). To visualize the RNA-probe binding, colorimetric reaction was performed for 1-2 days at room temperature in a solution containing NBT (nitro-blue tetrazolium chloride, Roche) and BCIP (5-bromo-4-chloro-30-indoly phosphate p-toluidine salt, Roche). After development, the sections were washed and mounted in Glycerol Jelly (Merck Millipore). Images were acquired with a Leica DFC550 camera into a Leica DM5000B microscope, Leica K5 camera into Leica DMi8 microscope or with an Axioscan Z1 widefield microscope (Zeiss).

Immunolabeling-enabled three-dimensional imaging of solvent-cleared organ (iDISCO+)

Whole mount for the iDISCO+ protocol was conducted following the previously described methods[51,52]. After perfusing mice with 4% PFA, heads (without any dissection) were dehydrated using a series of methanol concentrations (50, 80, 100, and 100%) and subsequently incubated overnight in 6% H_2O_2 in methanol to bleach the samples.

Following this, heads were blocked with PBS-GT (0.5% Triton X-100, 0.2% gelatin) for 4 days. For the clearing process, heads underwent dehydration in methanol (20, 40, 60, and 80%) at room temperature on a rotating shaker. Specimens were then immersed twice in 100% methanol for 1 hour and treated overnight in 1/3 volumes of 100% dichloromethane (DCM; Sigma-Aldrich; 270997). The subsequent day, heads were incubated in 100% DCM for 30 minutes. Finally, samples were cleared in 100% dibenzyl ether (DBE; Sigma-Aldrich; 108014) until they became translucent.

Ultramicroscopy and Image Processing

3D imaging was primarily performed with an ultramicroscope I (LaVision BioTec) using ImspectorPro software (LaVision BioTec). The light sheet was generated by a laser (wavelength 647 or 561 nm, LaVision BioTec). A binocular stereomicroscope (MXV10, Olympus) with a 23x objective (MVPLAPO, Olympus) was used at different magnifications (1.25x). Samples were placed in an imaging reservoir made of 100% quartz (LaVision BioTec) filled with ethyl cinnamate and illuminated from the side by the laser light.

Images were generated using Imaris x64 software (version 9.3.1, Bitplane). Stack images were first converted to Imaris files (.ims) using ImarisFileConverter. The whisker pad and upper lip areas reconstruction were generated by creating a mask around each one using the “surface tool” and they were pseudo-coloured (whisker pad area in magenta and upper lip area in cyan). Each individual follicle was isolated also manually using the same tool, selecting nine follicles arbitrarily at three different points from medial to lateral.

***In utero* and postnatal unilateral whisker pad cauterization**

Embryonic unilateral whisker pad cauterization (embWPC) was performed at E14 as described previously for enucleation[9]. Dams were deeply anesthetized with isoflurane and the uterine horns were exposed through a midline laparotomy. After cauterizing right whisker pad side in half of the litter, the embryos were returned to the abdominal cavity, the surgical incision was closed, and the embryos were allowed to develop until either E18 or postnatal stages. Postnatal unilateral whisker pad cauterization (P0WPC) was performed on P0 pups. Animals were deeply anaesthetized on ice. The right whisker pad was cauterized under the loupe to specifically burn the principal whiskers follicles. Pups were then warmed up to 37ºC on a heating pad, before being returned to the mother.

Measurement of brain areas and data analysis

ImageJ software was used to measure the size of individual barrels, barrel field territories in the cortex, thalamus and brainstem, as well as the snout areas in slices. For barrel field territories and snout areas data were normalized. Each barrel field or snout area from a given experimental condition was normalized to the corresponding barrel field or snout mean area in the control, which was considered as 1. For the snout measurements, the skin of the snout was flattened and post-fixed in 4% PFA. Paraffin slices of 5 μm were obtained to quantify the number of follicles and the upper lip snout area using Nissl staining. We measure two slices per animal, one medial and one more lateral, and calculated the average. TCA-GFP mouse was used for the quantifications of the barrel field definition in flattened tangential sections, barrel field areas *in toto* and thalamic territories in slices. To quantify the size of cortical areas *in toto*, TCA-GFP (control, embWPC, P0WPC, Th^{Kir} and embWPC-Th^{Kir}) mice were perfused and directly processed to obtain images under the stereo fluorescent microscope (Leica MZ10 F). Coronal serial slices of 80 μm were obtained from TCA-GFP brains, and thalamic barrel field territories were immunolabel with GFP and Vglut2 in order to better detect the areas. For $\Delta F_b/F_s$ quantifications, we used ImageJ to measure the gray value of EGFP labelling

in barrels of flattened tangential sections. $\Delta F_b/F_s$ was calculated using the maximum value of the baseline signal average as F_s in single barrels. To measure the gray value, we used a 20-width segmented line, covering 5 barrels per condition, and calculated the average. To compare the barrel profile for the different conditions, we normalized each barrel´s gray values to the lowest number (septa), which was considered as 0. Next, we took 11 gray value data points per barrel to normalize the length for all the conditions.

Dye-tracing studies

For axonal tracing, animals were perfused with 4% PFA in PBS. Heads were post-fixed overnight to trace innervation from the snout to the trigeminal nucleus, while brains were dissected and post-fixed overnight to trace thalamocortical axons. Small DiI (1,1′-dioctadecyl 3,3,3′,3′-tetramethylindocarbocyanine perchlorate; Invitrogen), DiA (4-[4-(dihexadecylamino) styryl]-N-methylpyridinium iodide; Invitrogen) and DiD (1,1'-Dioctadecyl-3,3,3',3'-Tetramethylindodicarbocyanine, 4-Chlorobenzenesulfonate Salt; Invitrogen) crystals were inserted under a stereo fluorescence microscope (MZ10 F, Leica) into the PMBSF, ALBSF, the whisker pad and upper lip. The dye was allowed to diffuse at 37 °C in PFA solution for 4 to 8 weeks to trace the innervation from the snout to the PrV. In order to trace the thalamocortical pathway, small DiI and DiA crystals were inserted into distinct PMBSF barrels (C2, C3, D3 and C4) and DiI, DiA and DiD crystals were placed into ALBSF territory. To reveal the PBMSF and ALBSF, a TCA-GFP transgenic specific mouse line was used. The dye was allowed to diffuse at 37 °C in PFA solution for 3 weeks. Vibratome sections (80 μm thick) were obtained and counterstained with the fluorescent nuclear dye DAPI (Sigma-Aldrich). Three sections per animal were imaged using a Leica K5 camera into Leica DMi8 microscope. Image analysis was performed on ImageJ. To quantify the translocation of the backlabeling in the VPM, the distance from the dorsolateral geniculate (dLG) nucleus border was measured to the center of the backlabeled cells in the VPM. The distance from the dLG nucleus border

to the separation between PMBSF and ALBSF was determined following the barreloids rows in the VPM of ctrl mice.

Measurement of PrV axons overlap in VPM and data analysis

To label rhombomere 3-derived vPrV neurons, we used the *Krox20*^{Cre} line[48] to drive the Rosa-Zsgreen reporter (*R26RZsGreen*)[53], whereas to label rhombomere 2-derived dPrV neurons, we used the *r2*^{mCherry} reporter line[18]. Brains from *Krox20*^{Cre}; *R26RZsGreen*; *r2*^{mCherry} animals, in which vPrV and dPrV projections are labeled simultaneously, were collected at embryonic stages (E16.5, E18.5) and postnatal stages (P0, P4, P8) for analysis. Embryonic brains were directly post-fixed in 4% PFA in PBS, while postnatal brains were perfused before post-fixation in the same fixative. Brains were cut on a Vibratome (Leica) at 60 μm thickness throughout the VPM and PrV. To enhance the r2::mCherry signal, the sections were stained with a rabbit anti-RFP primary antibody (1:1000, Rockland, 600-401-379) coupled to an anti-rabbit Alexa 568 secondary antibody (1:500, Invitrogen, A11011), while the endogenous Zsgreen fluorescence was not amplified. At least five sections per animal were imaged using Axioscan Z1 widefield microscope (Zeiss), using a 10x (NA=0.45) plan-APOCHROMAT objective. Subsequent image analysis was conducted using ImageJ. To quantify the percentage of overlap of vPrV-dPrV axons in the VPM, wand tool connecting pixels of the same intensity level in a 15-pixel range, was used to automatically delineate the innervation area of Krox20+ and R2+ axons, generating the Regions of Interest (ROIs). Subsequently, the overlapping area and the total innervation area of both Krox20+ and R2+ axons were measured with the measure tool in ImageJ to calculate the percentage of overlap of PrV axons in the VPM.

***In vivo* mesoscale calcium imaging**

As previously described[21], embryos at E18 were extracted from the uterus and maintained at 35 ºC. E18 pups were immobilized using soft clay. P4 mice underwent

anesthesia with ice, followed by surgical removal of the scalp. A 3D-printed plastic holder was attached to the skull using cyanoacrylate adhesive and dental cement, then affixed to a ball-joint holder to stabilize the head. To maintain body temperature, pups were placed on a controlled temperature heating pad, ensuring a range of 32-34 ºC. For recording calcium activity, we used a 16-bit CMOS camera (ORCA-Flash 4.0, Hamamatsu) coupled to a stereo microscope (Stereo Discovery V8, Zeiss), which offered 470 nm LED illumination. For *Emx1*^{GCaMP6f}, images were acquired with a frame size of 1024x1024 pixels using a macro magnification of 1.6x at E18 and of 1.25x at P4, resulting in spatial resolution of 8.12 µm/pixel and 10.64 µm/pixel, respectively. For *Snap25-GCaMP6f* mice at P4, images were acquired with a frame size of 1024x1024 pixels using a macro magnification of 1.6x, resulting in spatial resolution of 8.12 µm/pixel. Image frames were captured continuously at a rate of 3.33 frames per second (300 ms frame period) for *Emx1*^{GCaMP6f} and 10 frames per second (100 ms frame period) for *Snap25-GCaMP6f*, with an average of 3 movies was acquired per animal.

In vivo mechanical stimulation of the whisker pad

We conducted somatosensory stimulations by touching the whisker pad and upper lip using a 0.16 g von Frey filament (TouchTest®, BIOSEB). Each animal was stimulated at least three times, with intervals of 5 minutes between each stimulus. Subsequently, we calculated the size of responses in the PMBSF and ALBSF elicited by whisker pad and upper lip stimulations.

Analysis of the evoked activity *in vivo*

For the assignment of cortical territories, the perimeters of the PMBSF and ALBSF were determined using the cortical responses elicited by mechanical stimulation of five sites on the whisker pad, as previously described[20,21] and two sites of the upper lip. At embryonic day (E)18, the perimeters were predicted by scaling down and superimposing the limits of the sensory territories observed in the TCA-GFP transgenic line[13] at P2, as

previously detailed[21], and using the responses to whisker pad and upper lip stimulations as reference for PMBSF and ALBSF, respectively. Image analysis was performed with ImageJ. The mean fluorescence of five frames just prior to the stimulation established F0 (baseline fluorescence), and a $\Delta F/F0$ time series was then generated from the raw data and subsequently transformed into 8-bit images before processing with a 2-pixel diameter Gaussian filter. A maximum intensity projection of all frames containing evoked responses was obtained. The boundaries of the response were defined using the wand tool, connecting pixels of the same intensity level within a 15-pixel range, and the area of each response was calculated using the measure tool in ImageJ. To measure the active fraction of PMBSF and ALBSF in embWPC mice at E18 and P4, the control side was used to delineate the PMBSF and ALBSF territories following stimulation of the whisker pad or upper lip, respectively. On the WPC side, these areas were superimposed using the mirror image from the control side. The PMBSF and ALBSF active fractions were determined by measuring all elicited responses within each territory and calculating the percentage of the PMBSF and ALBSF theoretical areas occupied by these responses following whisker pad or upper lip stimulations. To quantify the percentage of overlap between responses following whisker pad and upper lip stimulations (%PMBSF-ALBSF overlap) at E18 and P4, the overlap between all elicited responses following whisker pad and those following upper lip stimulations was calculated. To quantify the percentage of overlap within PMBSF or ALBSF (% Responses overlap) in ctrl, embWPC and Th^{Kir}, the overlap for two different stimuli on the whisker pad or two different stimuli on the upper lip was calculated.

To visualize the evoked stimuli in different color profiles for the generation of supplementary movies, we utilized custom scripts developed in Matlab™. These scripts were adapted from the image analysis suite WholeBrainDX (referenced in the Data and code availability section). For each movie, frames containing movement artifacts, spontaneous activity, and calcium activity deemed as stimulation byproducts were excluded. Baseline correction was performed using the built-in Matlab function

'msbackadj' with a window size of 20 and a step size of 20. Subsequently, ΔF/F0 was computed using the median value of the corrected signal as F0. Movie segmentation and calcium event detection followed the method described[45]. Image segmentation and generation of a binary movie involved Gaussian smoothing with an 80 μm distance and a signal intensity threshold. The binary movie was color-labeled using ImageJ software and customized with a Gaussian filter. Subsequently, the original movie and the color-coded binary movie were merged using the 'Image Calculator' function in ImageJ.

Microdissection and RNA isolation for RNA-seq

To collect tissue from the PMBSF and ALBSF territories, ctrl and embWPC P0 pups were euthanized via decapitation, and their brains were dissected out under RNase-free conditions to prevent RNA degradation. The brains (five brains were pooled for each sample) were collected in ice-cold KREBS solution and sliced into 300 μm sections using a vibratome (VT1000S Leica). The PMBSF and ALBSF territories were rapidly microdissected under a stereo microscope. The bulk tissue was immediately transferred to lysis buffer of the Rneasy® Micro Kit (Qiagen, 74004) for total RNA extraction, following the manufacturer's instructions. RNA quality was measured for all samples using an Agilent Bioanalyzer 2100 system, and only samples with RNA Integrity Number (RIN) > 8 were used for library construction.

Library preparation and RNA sequencing

Library construction and sequencing were performed at Novogene Co. Ltd. Genomics core facility (Cambridge, UK). cDNA multiplex libraries were prepared using a custom Novogene NGS RNA Library Prep Set (PT042) kit. Briefly, mRNA was purified from total RNA using poly-T oligo-attached magnetic beads. After fragmentation, the first strand cDNA was synthesized using random hexamer primers followed by the second strand

cDNA synthesis. The library was ready after end repair, A-tailing, adapter ligation, size selection, amplification, and purification.

The library was checked with Qubit and real-time PCR for quantification and bioanalyzer for size distribution detection. Libraries were pooled and sequenced in 2x150bp paired-end mode on a S4 flowcell in the Illumina Novaseq6000 platform. A minimum of 40 million reads were generated from each library.

Bioinformatic analysis of the RNA-seq

RNA-seq analysis were performed as previously described[54] with minor modifications: quality control of the raw data was performed with FastQC (v.0.11.9). RNA-seq reads were mapped to the Mouse genome (GRCm39) using STAR (v2.7.9a)[55] and SAM/BAM files were further processed using SAMtools (v1.15). Aligned reads were counted and assigned to genes using Ensembl release 104 gene annotation and FeatureCounts, Subread (v2.0.1). Normalization of read counts and differential expression analyses were performed using DESeq2 (v1.32)[56], Bioconductor (v3.15)[57] in the R statistical computing and graphics platform (v4.2.2 “Innocent and Trusting”).

In the analysis of PMBSF and ALBSF datasets (control and embWPC samples) generated for this study, significantly Differentially Expressed Genes (DEGs) were identified using a simultaneous statistical significance threshold (Benjamini-Hochberg (BH) adjusted *P*-value < 0.1) and absolute log2 fold change (log2FC) > 0.14 by shrunken log2FC using the adaptive *T* prior Bayesian shrinkage estimator “apeglm” (**Tables S1** and **S2**)[58]. Hierarchical clustering analysis was performed using “Euclidean” distance and “Complete” clustering methods metrics to visualize significantly upregulated and down-regulated genes. Functional enrichment analyses were performed using clusterProfiler (v4.4.4)[59] under org.Mm.eg.db package (v3.15) for better annotation data. All enriched terms were considered significant at adjusted P-values by ‘BH’ < 0.1, in the Gene Ontology (GO) Over-Representation Analysis. Enrichment results were further

clustered and simplified using the simplifyEnrichment package (version 1.11.1)[60] (**Table S3)**.

Ex vivo calcium imaging

At E16, embryos were retrieved from the dam's uterus by cesarean section, their brains were rapidly dissected out and they were submerged in an ice-cold slicing solution containing (in mM): 2.5 KCl, 7 $MgSO_4$, 0.5 $CaCl_2$, 1 NaH_2PO_4, 26 Na_2HCO_3, 11 glucose and 228 sucrose. Coronal slices (350 μm thick) were obtained using a vibratome (VT1200S Leica) and they were left to recover for at least 30 minutes at room temperature in standard artificial cerebrospinal fluid (ACSF) containing (in mM): 119 NaCl, 5 KCl, 1.3 $MgSO_4$, 2.4 $CaCl_2$, 1 NaH_2PO_4, 26 Na_2HCO_3 and 11 glucose. All extracellular solutions were continuously bubbled with a 95% O_2 and 5% CO_2 gas mixture. Slices were loaded with the calcium indicator Cal520TM (AAT Bioquest) as previously described[9,20], transferred to a submersion-type recording chamber and perfused with warm ACSF (32-34 ºC) at a rate of 1.8 ml/min. Images were acquired with a digital charge-coupled device (CCD) camera (ORCA-R2 C10600-10B, Hamamatsu) coupled to an upright microscope (DM-LFSA, Leica) and using a 5x objective. For recordings of spontaneous calcium activity, frames were acquired with an exposure time of 150 ms, an interframe interval of 300 ms, a frame size of 672x512 pixel and a spatial resolution of 2.5 μm/pixel. With each slice, 1 to 5 epochs of 15 mins (3000 frames) were recorded.

Analysis of fluorescence spontaneous activity

Analysis of spontaneous thalamic calcium activity was conducted using custom software developed in Matlab™, which was adapted from the CalciumDX toolbox (indexed in the Data and code availability section). For each movie, VPM was delineated, and two areas (VPMlateral and VPMmedial) were subdivided into a grid of 6x6 pixels where each small square is a region of interest (ROI). Calcium activity events were detected based on the

average calcium signal of each ROI over time, employing threshold-based algorithms modified from CalciumDX. To identify significant synchronous activity and discard ROI co-activation that resulting from random temporal coincidence of calcium events, we generated surrogated calcium events sequences for each experiment using Matlab™. The alternative dataset was built by randomly shuffling the original temporal intervals between calcium transients in every ROI while preserving the spiking frequency and temporal structure of the calcium activity. Subsequently, the maximum value of co-activation from shuffled data was calculated. Through 1000 iterations, we established a synchronicity threshold as the 95th percentile of the maximum values of co-activation obtained from the shuffled dataset. In each experiment, only activity super passing the synchronicity threshold was used for calculations and visualization. The onset of a synchronic event was defined as the frame in which co-activation overpass the threshold, while the end was determined as the frame in which co-activation reached 25% of peak synchronicity.

Quantification and statistical analysis

Data were analysed using Prism 9 (GraphPad). A Kolmogorov-Smirnov normality test was conducted on all datasets. For independent data that conforming to a normal distribution, an unpaired two-tailed Student's *t*-test was employed to compare two groups. In cases where independent data that did not follow a normal distribution, a Mann-Whitney *U*-Test two-tailed test was used for comparison. For analyses involving more than two groups and one factor, one-way ANOVA was applied, followed by a Tukey *post hoc* analysis when data exhibited a normal distribution. For more than two groups and two factors, two-way ANOVA was conducted, followed by a Tukey *post hoc* analysis for normally distributed data. When data did not conform to a normal distribution, a Kruskal-Wallis test was performed, followed by Dunn's multiple comparisons without any correction. Results are presented as mean ± standard error of mean (SEM) with the n value for each dataset. Statistically significant effects and n numbers are detailed in the

corresponding figure legend or STAR Methods. The significance threshold was set at 0.05, two-tailed (not significant, ns, $p > 0.05$; *$p < 0.05$; ** $p < 0.01$; *** $p < 0.001$). No data exclusion was performed. Data for RNA-seq were processed according to the description in the STAR Methods sections, and statistical details are explained in the results and corresponding figure legends.

Tables

Table S1. Differential expression analysis of PMBSF vs ALBSF control samples from bulk RNA-seq. Related to Figures 3 and S6.

Table S2. Differential expression analysis of EmbWPC vs control-ALBSF samples from bulk RNA-seq. Related to Figures 3 and S7.

Table S3. Enrichment analysis of EmbWPC and control-ALBSF samples from bulk RNA-seq. Related to Figures 3 and S7.

Multimedia files

Video S1. iDISCO 3D reconstruction of E18 control mouse. Volume of the whisker pad and upper lip areas in magenta and cyan, respectively. Volume of nice whisker pad and nine upper lip follicles in yellow. Related to Figures 1A and S2D.

Video S2. iDISCO 3D reconstruction of E18 embWPC mouse. Volume of the whisker pad and upper lip areas in magenta and cyan, respectively. Volume of nice whisker pad and nine upper lip follicles in yellow. Related to Figures 1A and S2D.

Video S3. *In vivo* cortical evoked responses in the control side (ipsilateral to cauterization) of embWPC mouse at E18. Stimulations of the whisker pad (magenta) and upper lip (cyan). Dashed lines delineate cortical hemisphere, PMBSF and ALBSF putative cortical territories. Speed x3.3. Related to Figures 2A, 2B, 2D and 2E.

Video S4. *In vivo* cortical evoked responses in the whisker pad cauterized (WPC) side (contralateral to cauterization) of embWPC mouse at E18. Stimulations of the whisker pad (magenta) and upper lip (cyan). Dashed lines delineate cortical hemisphere, PMBSF and ALBSF putative cortical territories translated from control side stimulations ("PMBSF" and "ALBSF"). Speed x3.3. Related to Figures 2A, 2B, 2D and 2E.

Video S5. *In vivo* cortical evoked responses in the control side (ipsilateral to cauterization) of embWPC mouse at P4. Stimulations of the whisker pad (magenta) and upper lip (cyan). Dashed lines delineate cortical hemisphere, PMBSF and ALBSF cortical territories. Speed x3.3. Related to Figures 2A, 2C, 2D and 2E.

Video S6. *In vivo* cortical evoked responses in the whisker pad cauterized (WPC) side (contralateral to cauterization) of embWPC mouse at P4. Stimulations of the whisker pad (magenta) and upper lip (cyan). Dashed lines delineate cortical hemisphere, PMBSF and ALBSF cortical territories translated from control side stimulations ("PMBSF" and "ALBSF"). Speed x3.3. Related to Figures 2A, 2C, 2D and 2E.

Video S7. Topographic representations in the cortex of *in vivo* evoked responses in control mouse at P4. Stimulations of the whisker pad (magenta, blue, green, yellow and orange) and upper lip (cyan and white). Dashed lines delineate cortical hemisphere, PMBSF and ALBSF evoked cortical territories. Speed x3.3. Related to Figures 2F and 2G.

Video S8. Topographic representations in the cortex of *in vivo* evoked responses in control mouse at E18. Stimulations of the whisker pad (magenta, blue, green, yellow and orange) and upper lip (cyan and white). Dashed lines delineate cortical hemisphere, PMBSF and ALBSF evoked putative territories in the cortex. Speed x3.3. Related to Figures 2F and 2G.

Video S9. Topographic representations in the cortex of *in vivo* evoked responses in embWPC mouse at P4. Stimulations of the upper lip (cyan and white). Dashed lines delineate cortical hemisphere and ALBSF evoked cortical territory. Speed x3.3. Related to Figures 2F and 2G.

Video S10. Topographic representations in the cortex of *in vivo* evoked responses in embWPC mouse at E18. Stimulations of the upper lip (cyan and white). Dashed lines delineate cortical hemisphere and ALBSF evoked cortical territory. Speed x3.3. Related to Figures 2F and 2G.

Video S11. Spontaneous thalamic activity in the VPM regions (VPMlat, lateral; and VPMmed, medial) in acute slice of control mice at E16. Dashed lines delineate dLG (dorsolateral geniculate) nucleus, VPMlat and VPMmed. Speed x15. Related to Figures 4B and 4C.

Video S12. Spontaneous thalamic activity in the VPM regions (VPMlat, lateral; and VPMmed, medial) in acute slice of embWPC mice at E16. Dashed lines delineate dLG (dorsolateral geniculate) nucleus, VPMlat and VPMmed. Speed x15. Related to Figures 4B and 4C.

Video S13. Topographic representations in the cortex of *in vivo* evoked responses in control mouse at P4. Stimulations of the whisker pad (magenta, blue, green, yellow and orange) and upper lip (cyan and white). Dashed lines delineate cortical hemisphere, PMBSF and ALBSF evoked cortical territories. Speed x1. Related to Figure 4E.

Video S14. Topographic representations in the cortex of *in vivo* evoked responses in Th^{Kir} mouse at P4. Stimulations of the whisker pad (magenta, blue, green, yellow and

orange) and upper lip (cyan and white). Dashed lines delineate cortical hemisphere, PMBSF and ALBSF evoked cortical territories. Speed x1. Related to Figure 4E.

Key resources table

REAGENT or RESOURCE	SOURCE	IDENTIFIER
Antibodies		
Guinea pig polyclonal anti-vGlut2	Synaptic Systems	Cat# 135 404, RRID:AB_887884
Chicken polyclonal anti-GFP	Aves Labs	Cat# GFP-1020, RRID:AB_10000240
Rat monoclonal anti-RFP	ChromoTek	Cat# 5f8-100 (also rfp-antibody-5f8), RRID:AB_2336064
Rabbit polyclonal anti-RFP	Rockland	Cat# 600-401-379, RRID:AB_2209751
Donkey polyclonal anti-guinea pig IgG Alexa Fluor 488	Thermo Fisher Scientific	Cat# A-11073, RRID:AB_2534117
Goat polyclonal anti-chicken IgY Alexa Fluor 488	Thermo Fisher Scientific	Cat# A-11039, RRID:AB_2534096
Donkey polyclonal anti-rat IgG Alexa Fluor 594	Thermo Fisher Scientific	Cat# A-21209, RRID:AB_2535795
Goat anti-rabbit IgG Alexa Fluor 568	Invitrogen	Cat# A-11011 (also A11011, A 11011), RRID:AB_143157
Chemicals, peptides, and recombinant proteins		
Tamoxifen	Sigma-Aldrich	Cat# T5648
Corn oil	Sigma-Aldrich	Cat# C8267
DiI (1,1′-dioctadecyl 3,3,3′,3′-tetramethylindocarbocyanine perchlorate)	Invitrogen by Thermo Fisher Scientific	Cat# D3911
DiA (4-[4-(dihexadecylamino) styryl]-N-methylpyridinium iodide)	Invitrogen by Thermo Fisher Scientific	Cat# D3883
DiD (1,1'-Dioctadecyl-3,3,3',3'-Tetramethylindodicarbocyanine, 4-Chlorobenzenesulfonate Salt)	Invitrogen by Thermo Fisher Scientific	Cat# D7757
Cytochrome c	Sigma-Aldrich	Cat# C2506
DAB (3-3′ diaminobenzidine tetrahydrochloride hydrate)	Sigma-Aldrich	Cat# D5637
Cresyl Violet acetate	Sigma-Aldrich	Cat# C5042
Xylen	Sigma-Aldrich	Cat# 534056
Paraformadehyde	Avantor	Cat# J531
BSA	Sigma-Aldrich	Cat# A7906
Triton X-100	Sigma-Aldrich	Cat# T8787
NBT (nitro-blue tetrazolium chloride)	Roche	Cat# 11383213001
BCIP (5-bromo-4-chloro-30-indoly phosphate p-toluidine salt)	Roche	Cat# 16670
Alkaline phosphatase-conjugated anti-digoxigenin antibody	Roche	Cat# 11093274910
DCM (dichloromethane)	Sigma-Aldrich	Cat# 270997

BDE (dibenzyl ether)	Sigma-Aldrich	Cat# 108014
Cal520TM	AAT Bioquest	Cat# 21130
Fluoromount	Sigma-Aldrich	Cat# F4680
Glycerol Jelly	Merck Millipore	Cat# 1086350100
Eukitt	Merck Millipore	Cat# 3989
DAPI	Sigma-Aldrich	Cat# D9542
Progesterone	Pfizer	Cat# DEPO-PROGEVERA®
Isoflurane	Zoetis	Cat# 1001055
Critical commercial assays		
RNeasy® Micro Kit	Qiagen	Cat# 74004
Deposited data		
Bulk RNAseq	This study	not available until peer review publication
Experimental models: Organisms/strains		
Mouse: ICR/CD-1 WT	The Jackson Laboratory	RRID:MGI:5649797
Mouse: TCA-GFP Tg	Mizuno, H. et al.[11]	RBRC10599
Mouse: R26Kir2.1-mCherry	Moreno-Juan et al.[9]	MGI:6191641
Mouse: Emx1Cre/+	The Jackson Laboratory	RRID:IMSR_JAX:005628
Mouse: R26GCaMP6f	The Jackson Laboratory	RRID:IMSR_JAX:024105
Mouse: Gbx2$^{CreERT2/+}$	The Jackson Laboratory	RRID:IMSR_JAX:022135
Mouse: *r2*^{mCherry}	Bechara, A. et al.[18]	N/A
Mouse: Krox20Cre	Voiculescu O. et al.[48]	N/A
Mouse: *R26RZsGreen*	The Jackson Laboratory	RRID:IMSR_JAX:007906
Mouse: Snap25-GCaMP6f	The Jackson Laboratory	RRID:IMSR_JAX:025111
Software and algorithms		
MATLAB	MathWorks	RRID:SCR_001622
CalciumDX	https://github.com/ackman678/CalciumDX	N/A
WholeBrainDX	Ackman et al.[45]	https://github.com/ackman678/wholeBrainDX
Graphpad Prism 9	GraphPad	RRID:SCR_002798
Fiji	http://fiji.sc	RRID:SCR_002285
IMARIS x64 (version 9.3.1)	Bitplane	RRID:SCR_007370
Adobe Photoshop	Adobe Systems	RRID:SCR_014199
Adobe Illustrator	Adobe Systems	RRID:SCR_010279
ImSpectorPro software	LaVision BioTec	N/A
FastQC v0.11.9	Babraham Institute	RRID:SCR_014583
STAR (v.2.7.9a)	Dobin et al.[55]	https://github.com/alexdobin/STAR RRID:SCR_004463

Samtools (v1.15)	http://htslib.org/	RRID:SCR_002105
subread v2.0.1	subread.sourceforge.net/featureCounts.html	RRID:SCR_009803
R (4.2.2)	R Project for Statistical Computing	https://www.r-project.org/ RRID:SCR_001905
Bioconductor (v3.15)	Huber et al.[57]	*http://www.bioconductor.org/ RRID:SCR_006442*
DESeq2 v1.32.0	Love et al.[56]	RRID:SCR_015687
clusterProfiler (v4.4.4)	Yu et al.[60]	*http://bioconductor.org/packages/release/bioc/html/clusterProfiler.html RRID:SCR_016884*
org.Mm.eg.db (v3.15)	https://bioconductor.org/packages/org.Mm.eg.db/	RRID:SCR_023488
Other		
Von Frey filament TouchTest®	BIOSEB	Cat# BIO-VF-M
Bioanalyzer 2100 system	Agilent	RRID:SCR_019715
NovaSeq6000	Illumina	RRID:SCR_016387
Vibratome VT1000S	Leica	RRID:SCR_016495
Vibratome VT1200S	Leica	RRID:SCR_018453
Cryotome HM400 E	MICROM	N/A
Microtome HM340 E	MICROM	N/A
Stereomicroscope SteREO Discovery.V8	Zeiss	https://www.micro-shop.zeiss.com/es/es/system/stereo+discovery-stereo+discovery.v8-estereomicroscopios/10156/
Stereo fluorescent microscope MZ10 F	Leica	https://www.leica-microsystems.com/products/light-microscopes/stereo-microscopes/p/leica-mz10-f/
DM5000B microscope	Leica	https://www.leica-microsystems.com/es/productos/microscopios-opticos/p/leica-dm5000-b/
DMi8 microscope	Leica	https://www.leica-microsystems.com/es/productos/microscopios-opticos/p/leica-dmi8-id/
Axioscan Z1 widefield microscope	Zeiss	RRID:SCR_020927
Microscope DM-LFSA	Leica	RRID:SCR_024857
Ultramicroscope I	LaVision BioTec	N/A

References

1. O'Leary, D.D., and Sahara, S. (2008). Genetic regulation of arealization of the neocortex. Curr Opin Neurobiol *18*, 90-100. 10.1016/j.conb.2008.05.011.
2. Rakic, P. (1988). Specification of cerebral cortical areas. Science *241*, 170-176. 10.1126/science.3291116.
3. O'Leary, D.D., Chou, S.J., and Sahara, S. (2007). Area patterning of the mammalian cortex. Neuron *56*, 252-269. 10.1016/j.neuron.2007.10.010.
4. Harris, K.D., and Shepherd, G.M. (2015). The neocortical circuit: themes and variations. Nat Neurosci *18*, 170-181. 10.1038/nn.3917.
5. Welker, C. (1976). Receptive fields of barrels in the somatosensory neocortex of the rat. J Comp Neurol *166*, 173-189. 10.1002/cne.901660205.
6. Diamond, M.E., von Heimendahl, M., Knutsen, P.M., Kleinfeld, D., and Ahissar, E. (2008). 'Where' and 'what' in the whisker sensorimotor system. Nat Rev Neurosci *9*, 601-612. 10.1038/nrn2411.
7. Brecht, M., Preilowski, B., and Merzenich, M.M. (1997). Functional architecture of the mystacial vibrissae. Behav Brain Res *84*, 81-97. 10.1016/s0166-4328(97)83328-1.
8. Woolsey, T.A., and Van der Loos, H. (1970). The structural organization of layer IV in the somatosensory region (SI) of mouse cerebral cortex. The description of a cortical field composed of discrete cytoarchitectonic units. Brain Res *17*, 205-242. 10.1016/0006-8993(70)90079-x.
9. Moreno-Juan, V., Filipchuk, A., Anton-Bolanos, N., Mezzera, C., Gezelius, H., Andres, B., Rodriguez-Malmierca, L., Susin, R., Schaad, O., Iwasato, T., et al. (2017). Prenatal thalamic waves regulate cortical area size prior to sensory processing. Nat Commun *8*, 14172. 10.1038/ncomms14172.
10. Lopez-Bendito, G., Anibal-Martinez, M., and Martini, F.J. (2022). Cross-Modal Plasticity in Brains Deprived of Visual Input Before Vision. Annu Rev Neurosci *45*, 471-489. 10.1146/annurev-neuro-111020-104222.
11. Gaspar, P., and Erzurumlu, R. (2013). The Birth of the Barrels. Developmental Cell *27*, 3-4. 10.1016/j.devcel.2013.09.028.
12. Erzurumlu, R.S., and Gaspar, P. (2020). How the Barrel Cortex Became a Working Model for Developmental Plasticity: A Historical Perspective. The Journal of Neuroscience *40*, 6460-6473. 10.1523/jneurosci.0582-20.2020.
13. Mizuno, H., Luo, W., Tarusawa, E., Saito, Y.M., Sato, T., Yoshimura, Y., Itohara, S., and Iwasato, T. (2014). NMDAR-regulated dynamics of layer 4 neuronal dendrites during thalamocortical reorganization in neonates. Neuron *82*, 365-379. 10.1016/j.neuron.2014.02.026.
14. Laumonnerie, C., Bechara, A., Vilain, N., Kurihara, Y., Kurihara, H., and Rijli, F.M. (2015). Facial whisker pattern is not sufficient to instruct a whisker-related topographic map in the mouse somatosensory brainstem. Development *142*, 3704-3712. 10.1242/dev.128736.
15. Ozdinler, P.H., and Erzurumlu, R.S. (2002). Slit2, a branching-arborization factor for sensory axons in the Mammalian CNS. J Neurosci *22*, 4540-4549. 10.1523/JNEUROSCI.22-11-04540.2002.
16. Oury, F., Murakami, Y., Renaud, J.S., Pasqualetti, M., Charnay, P., Ren, S.Y., and Rijli, F.M. (2006). Hoxa2- and rhombomere-dependent development of the mouse facial somatosensory map. Science *313*, 1408-1413. 10.1126/science.1130042.

17. Kitazawa, T., and Rijli, F.M. (2018). Barrelette map formation in the prenatal mouse brainstem. Curr Opin Neurobiol *53*, 210-219. 10.1016/j.conb.2018.09.008.
18. Bechara, A., Laumonnerie, C., Vilain, N., Kratochwil, C.F., Cankovic, V., Maiorano, N.A., Kirschmann, M.A., Ducret, S., and Rijli, F.M. (2015). Hoxa2 Selects Barrelette Neuron Identity and Connectivity in the Mouse Somatosensory Brainstem. Cell Rep *13*, 783-797. 10.1016/j.celrep.2015.09.031.
19. Zembrzycki, A., Chou, S.J., Ashery-Padan, R., Stoykova, A., and O'Leary, D.D. (2013). Sensory cortex limits cortical maps and drives top-down plasticity in thalamocortical circuits. Nat Neurosci *16*, 1060-1067. 10.1038/nn.3454.
20. Anton-Bolanos, N., Sempere-Ferrandez, A., Guillamon-Vivancos, T., Martini, F.J., Perez-Saiz, L., Gezelius, H., Filipchuk, A., Valdeolmillos, M., and Lopez-Bendito, G. (2019). Prenatal activity from thalamic neurons governs the emergence of functional cortical maps in mice. Science *364*, 987-990. 10.1126/science.aav7617.
21. Guillamon-Vivancos, T., Anibal-Martinez, M., Puche-Aroca, L., Moreno-Bravo, J.A., Valdeolmillos, M., Martini, F.J., and Lopez-Bendito, G. (2022). Input-dependent segregation of visual and somatosensory circuits in the mouse superior colliculus. Science *377*, 845-850. 10.1126/science.abq2960.
22. Martini, F.J., Moreno-Juan, V., Filipchuk, A., Valdeolmillos, M., and Lopez-Bendito, G. (2018). Impact of thalamocortical input on barrel cortex development. Neuroscience *368*, 246-255. 10.1016/j.neuroscience.2017.04.005.
23. Nakagawa, Y., and O'Leary, D.D. (2003). Dynamic patterned expression of orphan nuclear receptor genes RORalpha and RORbeta in developing mouse forebrain. Dev Neurosci *25*, 234-244. 10.1159/000072271.
24. Yuge, K., Kataoka, A., Yoshida, A.C., Itoh, D., Aggarwal, M., Mori, S., Blackshaw, S., and Shimogori, T. (2011). Region-specific gene expression in early postnatal mouse thalamus. J Comp Neurol *519*, 544-561. 10.1002/cne.22532.
25. Ebisu, H., Iwai-Takekoshi, L., Fujita-Jimbo, E., Momoi, T., and Kawasaki, H. (2017). Foxp2 Regulates Identities and Projection Patterns of Thalamic Nuclei During Development. Cereb Cortex *27*, 3648-3659. 10.1093/cercor/bhw187.
26. Puelles, L., Sanchez, M.P., Spreafico, R., and Fairen, A. (1992). Prenatal development of calbindin immunoreactivity in the dorsal thalamus of the rat. Neuroscience *46*, 135-147. 10.1016/0306-4522(92)90013-r.
27. Vitalis, T., Dauphinot, L., Gressens, P., Potier, M.C., Mariani, J., and Gaspar, P. (2018). RORalpha Coordinates Thalamic and Cortical Maturation to Instruct Barrel Cortex Development. Cereb Cortex *28*, 3994-4007. 10.1093/cercor/bhx262.
28. Van der Loos, H., and Woolsey, T.A. (1973). Somatosensory cortex: structural alterations following early injury to sense organs. Science *179*, 395-398. 10.1126/science.179.4071.395.
29. Killackey, H.P., and Belford, G.R. (1979). The formation of afferent patterns in the somatosensory cortex of the neonatal rat. J Comp Neurol *183*, 285-303. 10.1002/cne.901830206.
30. Woolsey, T.A., Anderson, J.R., Wann, J.R., and Stanfield, B.B. (1979). Effects of early vibrissae damage on neurons in the ventrobasal (VB) thalamus of the mouse. J Comp Neurol *184*, 363-380. 10.1002/cne.901840210.

31. Belford, G.R., and Killackey, H.P. (1979). The development of vibrissae representation in subcortical trigeminal centers of the neonatal rat. J Comp Neurol *188*, 63-74. 10.1002/cne.901880106.
32. Woolsey, T.A., and Wann, J.R. (1976). Areal changes in mouse cortical barrels following vibrissal damage at different postnatal ages. J Comp Neurol *170*, 53-66. 10.1002/cne.901700105.
33. Killackey, H.P., Belford, G., Ryugo, R., and Ryugo, D.K. (1976). Anomalous organization of thalamocortical projections consequent to vibrissae removal in the newborn rat and mouse. Brain Res *104*, 309-315. 10.1016/0006-8993(76)90623-5.
34. Renier, N., Dominici, C., Erzurumlu, R.S., Kratochwil, C.F., Rijli, F.M., Gaspar, P., and Chedotal, A. (2017). A mutant with bilateral whisker to barrel inputs unveils somatosensory mapping rules in the cerebral cortex. Elife *6*. 10.7554/eLife.23494.
35. Kleinfeld, D., Ahissar, E., and Diamond, M.E. (2006). Active sensation: insights from the rodent vibrissa sensorimotor system. Curr Opin Neurobiol *16*, 435-444. 10.1016/j.conb.2006.06.009.
36. Land, P.W., and Simons, D.J. (1985). Cytochrome oxidase staining in the rat SmI barrel cortex. J Comp Neurol *238*, 225-235. 10.1002/cne.902380209.
37. Jan, T.A., Lu, L., Li, C.X., Williams, R.W., and Waters, R.S. (2008). Genetic analysis of posterior medial barrel subfield (PMBSF) size in somatosensory cortex (SI) in recombinant inbred strains of mice. BMC Neurosci *9*, 3. 10.1186/1471-2202-9-3.
38. Grant, R.A., Sperber, A.L., and Prescott, T.J. (2012). The role of orienting in vibrissal touch sensing. Front Behav Neurosci *6*, 39. 10.3389/fnbeh.2012.00039.
39. Kuruppath, P., Gugig, E., and Azouz, R. (2014). Microvibrissae-based texture discrimination. J Neurosci *34*, 5115-5120. 10.1523/JNEUROSCI.4217-13.2014.
40. Morita, T., Kang, H., Wolfe, J., Jadhav, S.P., and Feldman, D.E. (2011). Psychometric curve and behavioral strategies for whisker-based texture discrimination in rats. PLoS One *6*, e20437. 10.1371/journal.pone.0020437.
41. Belford, G.R., and Killackey, H.P. (1980). The sensitive period in the development of the trigeminal system of the neonatal rat. J Comp Neurol *193*, 335-350. 10.1002/cne.901930203.
42. Dufour, A., Seibt, J., Passante, L., Depaepe, V., Ciossek, T., Frisen, J., Kullander, K., Flanagan, J., Polleux, F., and Vanderhaeghen, P. (2003). Area specificity and topography of thalamocortical projections are controlled by ephrin/Eph genes. Neuron *39*, 453-465. S0896627303004409 [pii].
43. Martini, F.J., Guillamon-Vivancos, T., Moreno-Juan, V., Valdeolmillos, M., and Lopez-Bendito, G. (2021). Spontaneous activity in developing thalamic and cortical sensory networks. Neuron *109*, 2519-2534. 10.1016/j.neuron.2021.06.026.
44. Mire, E., Mezzera, C., Leyva-Díaz, E., Paternain, A.V., Squarzoni, P., Bluy, L., Castillo-Paterna, M., López, M.J., Peregrín, S., Tessier-Lavigne, M., et al. (2012). Spontaneous activity regulates Robo1 transcription to mediate a switch in thalamocortical axon growth. Nat Neurosci *15*, 1134-1143. 10.1038/nn.3160.
45. James B. Ackman, H.Z., Michael C. Crair (2014). Structured dynamics of neural activity across developing neocortex. Preprint at bioRxiv. 10.1101/012237.

46. Gorski, J.A., Talley, T., Qiu, M., Puelles, L., Rubenstein, J.L., and Jones, K.R. (2002). Cortical excitatory neurons and glia, but not GABAergic neurons, are produced in the Emx1-expressing lineage. J Neurosci *22*, 6309-6314. 10.1523/JNEUROSCI.22-15-06309.2002.
47. Chen, L., Guo, Q., and Li, J. (2009). Transcription factor Gbx2 acts cell-nonautonomously to regulate the formation of lineage-restriction boundaries of the thalamus. Development *136*, 1317-1326. 10.1242/dev.030510.
48. Voiculescu, O., Charnay, P., and Schneider-Maunoury, S. (2000). Expression pattern of a Krox-20/Cre knock-in allele in the developing hindbrain, bones, and peripheral nervous system. Genesis *26*, 123-126. 10.1002/(sici)1526-968x(200002)26:2<123::aid-gene7>3.0.co;2-o.
49. Madisen, L., Garner, A.R., Shimaoka, D., Chuong, A.S., Klapoetke, N.C., Li, L., van der Bourg, A., Niino, Y., Egolf, L., Monetti, C., et al. (2015). Transgenic mice for intersectional targeting of neural sensors and effectors with high specificity and performance. Neuron *85*, 942-958. 10.1016/j.neuron.2015.02.022.
50. Franco, S.J., Gil-Sanz, C., Martinez-Garay, I., Espinosa, A., Harkins-Perry, S.R., Ramos, C., and Muller, U. (2012). Fate-restricted neural progenitors in the mammalian cerebral cortex. Science *337*, 746-749. 10.1126/science.1223616.
51. Renier, N., Wu, Z., Simon, D.J., Yang, J., Ariel, P., and Tessier-Lavigne, M. (2014). iDISCO: a simple, rapid method to immunolabel large tissue samples for volume imaging. Cell *159*, 896-910. 10.1016/j.cell.2014.10.010.
52. Renier, N., Adams, E.L., Kirst, C., Wu, Z., Azevedo, R., Kohl, J., Autry, A.E., Kadiri, L., Umadevi Venkataraju, K., Zhou, Y., et al. (2016). Mapping of Brain Activity by Automated Volume Analysis of Immediate Early Genes. Cell *165*, 1789-1802. 10.1016/j.cell.2016.05.007.
53. Madisen, L., Zwingman, T.A., Sunkin, S.M., Oh, S.W., Zariwala, H.A., Gu, H., Ng, L.L., Palmiter, R.D., Hawrylycz, M.J., Jones, A.R., et al. (2010). A robust and high-throughput Cre reporting and characterization system for the whole mouse brain. Nat Neurosci *13*, 133-140. 10.1038/nn.2467.
54. Herrero-Navarro, A., Puche-Aroca, L., Moreno-Juan, V., Sempere-Ferrandez, A., Espinosa, A., Susin, R., Torres-Masjoan, L., Leyva-Diaz, E., Karow, M., Figueres-Onate, M., et al. (2021). Astrocytes and neurons share region-specific transcriptional signatures that confer regional identity to neuronal reprogramming. Sci Adv *7*. 10.1126/sciadv.abe8978.
55. Dobin, A., Davis, C.A., Schlesinger, F., Drenkow, J., Zaleski, C., Jha, S., Batut, P., Chaisson, M., and Gingeras, T.R. (2013). STAR: ultrafast universal RNA-seq aligner. Bioinformatics *29*, 15-21. 10.1093/bioinformatics/bts635.
56. Love, M.I., Huber, W., and Anders, S. (2014). Moderated estimation of fold change and dispersion for RNA-seq data with DESeq2. Genome Biol *15*, 550. 10.1186/s13059-014-0550-8.
57. Huber, W., Carey, V.J., Gentleman, R., Anders, S., Carlson, M., Carvalho, B.S., Bravo, H.C., Davis, S., Gatto, L., Girke, T., et al. (2015). Orchestrating high-throughput genomic analysis with Bioconductor. Nat Methods *12*, 115-121. 10.1038/nmeth.3252.
58. Zhu, A., Srivastava, A., Ibrahim, J.G., Patro, R., and Love, M.I. (2019). Nonparametric expression analysis using inferential replicate counts. Nucleic Acids Res *47*, e105. 10.1093/nar/gkz622.

59. Gu, Z., and Hubschmann, D. (2023). simplifyEnrichment: A Bioconductor Package for Clustering and Visualizing Functional Enrichment Results. Genomics Proteomics Bioinformatics *21*, 190-202. 10.1016/j.gpb.2022.04.008.
60. Yu, G., Wang, L.G., Han, Y., and He, Q.Y. (2012). clusterProfiler: an R package for comparing biological themes among gene clusters. OMICS *16*, 284-287. 10.1089/omi.2011.0118.

Supplemental Figures

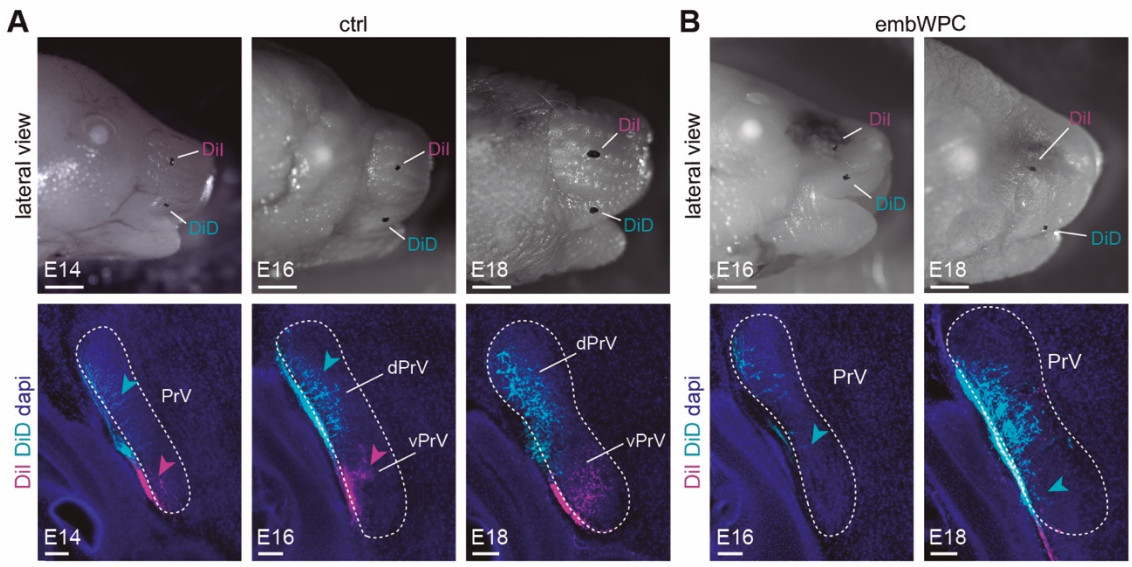

Figure S1. Early reorganization of peripheral axons at the trigeminal nucleus, Related to Figure 1. (A) Upper panels, lateral views of control mouse heads showing DiI and DiD crystal placements in the whisker pad and upper lip, respectively, at distinct developmental stages (E14, E16 and E18). Lower panels, coronal sections showing labelled axons at the vPrV (magenta, arrowheads) and dPrV (cyan, arrowheads) (n= 6 mice at E14, n= 9 mice at E16, n= 6 mice at E18). **(B)** Upper panels, lateral views of embWPC mouse heads showing DiI and DiD crystal placements in the whisker pad and upper lip, respectively, at distinct developmental stages (E16 and E18). Lower panels, coronal sections showing displaced upper lip axons at the vPrV (cyan, arrowheads) (n= 9 embWPC mice at E16, n= 5 embWPC mice at E18). E, embryonic; embWPC, embryonic whisker pad cauterized; PrV, principal nucleus; vPrV, ventral principal nucleus; dPrV, dorsal principal nucleus; DiI, 1,1′-dioctadecyl 3,3,3′,3′-tetramethylindocarbocyanine perchlorate; DiD, 1,1'-Dioctadecyl-3,3,3',3'-Tetramethylindodicarbocyanine, 4-Chlorobenzenesulfonate. Scale bars, (top) (A) and (B) 1000 μm; (bottom) (A) and (B) 100 μm.

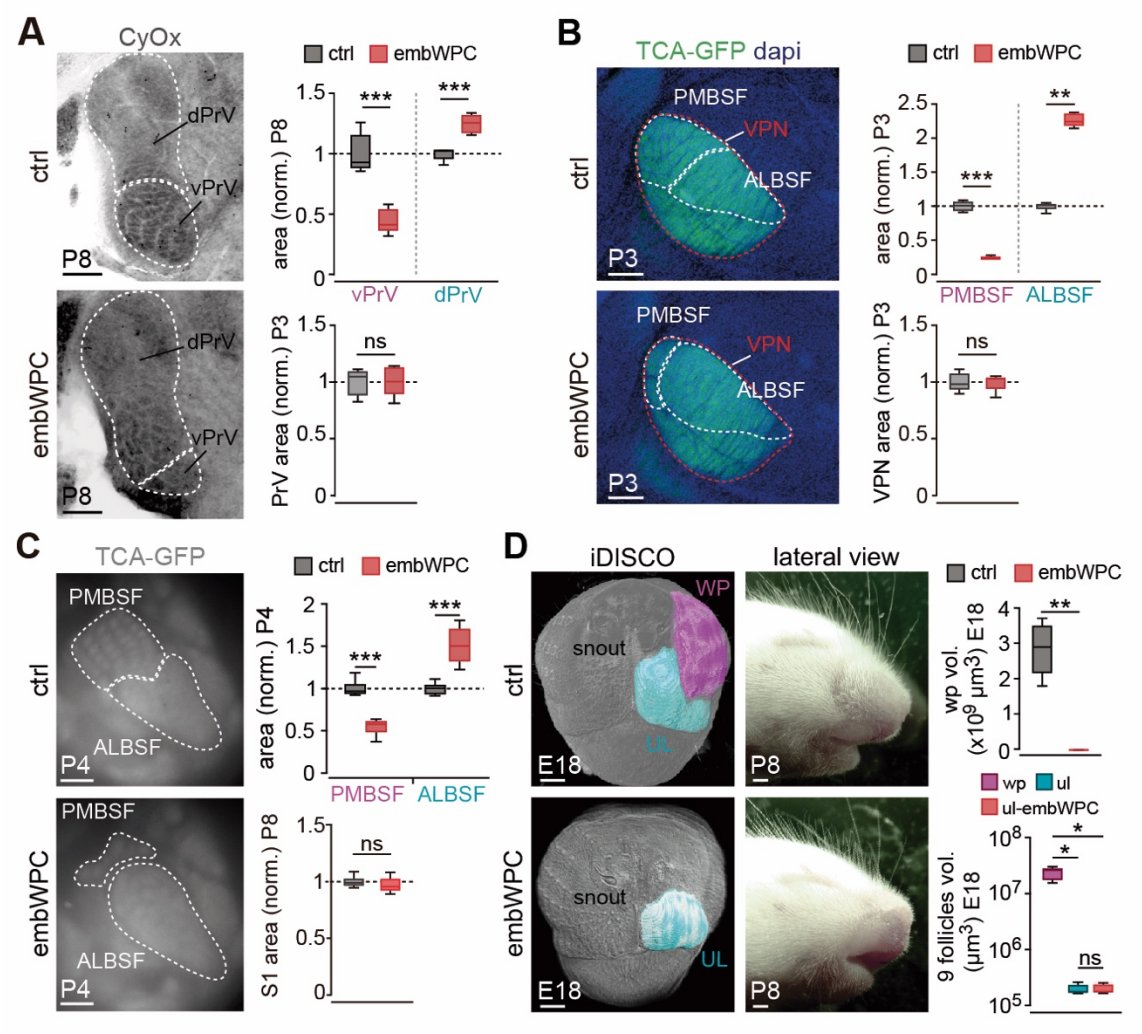

Figure S2. Intra-modal reorganization of facial whiskers representations in cortical and subcortical territories in embWPC mice, Related to Figures 1 and 2. (A) Coronal sections of the trigeminal PrV nucleus stained with CyOx in control and embWPC at P8. Quantification of the data (vPrV and dPrV areas, n= 5 ctrl mice, n= 5 embWPC mice, unpaired two-tailed Student *t*-test; PrV area, n= 5 ctrl mice, n= 5 embWPC mice, unpaired two-tailed Student *t*-test. ns, p > 0.9). **(B)** Coronal sections showing TCA-GFP labelling in the PMBSF, ALBSF and VPN of the thalamus in control and embWPC at P3. Quantification of the data (n= 5 ctrl mice, n= 5 embWPC mice, PMBSF, unpaired two-tailed Student *t*-test. ALBSF, Mann-Whitney *U*-test; VPN at P3, n= 5 ctrl mice, n= 5 embWPC mice, Mann-Whitney *U*-test. ns, p > 0.99). **(C)** Surface view of thalamocortical terminals (TCA-GFP+) in the cortical PMBSF and ALBSF in control and embWPC mice at P4. Quantification of the data (n= 6 ctrl mice, n= 6 embWPC mice, unpaired two-tailed Student *t*-test; S1 area at P8, n= 8 ctrl mice, n= 9 embWPC mice, unpaired two-tailed Student *t*-test. ns, p= 0.29). **(D)** Left, frontal snout iDISCO pictures showing the whisker pad (magenta) and upper lip (cyan) areas reconstruction for control and embWPC mice at E18. Right, Mouse heads showing the snout of control and embWPC at P8. Quantification of the iDISCO data (whisker pad volume at E18, n= 5 ctrl mice, n= 5 embWPC mice, Mann-Whitney *U*-test; 9 follicles volume at E18, n= 5 ctrl mice for wp and ul, n= 5 embWPC mice for ul-embWPC, Kruskal-Wallis test, **p < 0.01. Dunn's multiple comparison test post-hoc analysis, ns, p > 0.99). CyOx, Cytochrome oxidase; P, postnatal; WP, whisker pad; UL, upper lip; VPN, ventroposterior nucleus; TCA-GFP, thalamocortical axons labelled with green fluorescent protein; PMBSF, postero-medial barrel subfield; ALBSF, antero-lateral barrel subfield; S1, primary somatosensory cortex;

norm., normalized. Scale bars, (A) and (B) 200 μm; (C) and (D) (left) 500 μm; (D) (right) 1000 μm. Boxplots show the medians with the interquartile range (box) and range (whiskers). ns, not significant. *$p < 0.05$, **$p < 0.01$ ***$p < 0.001$.

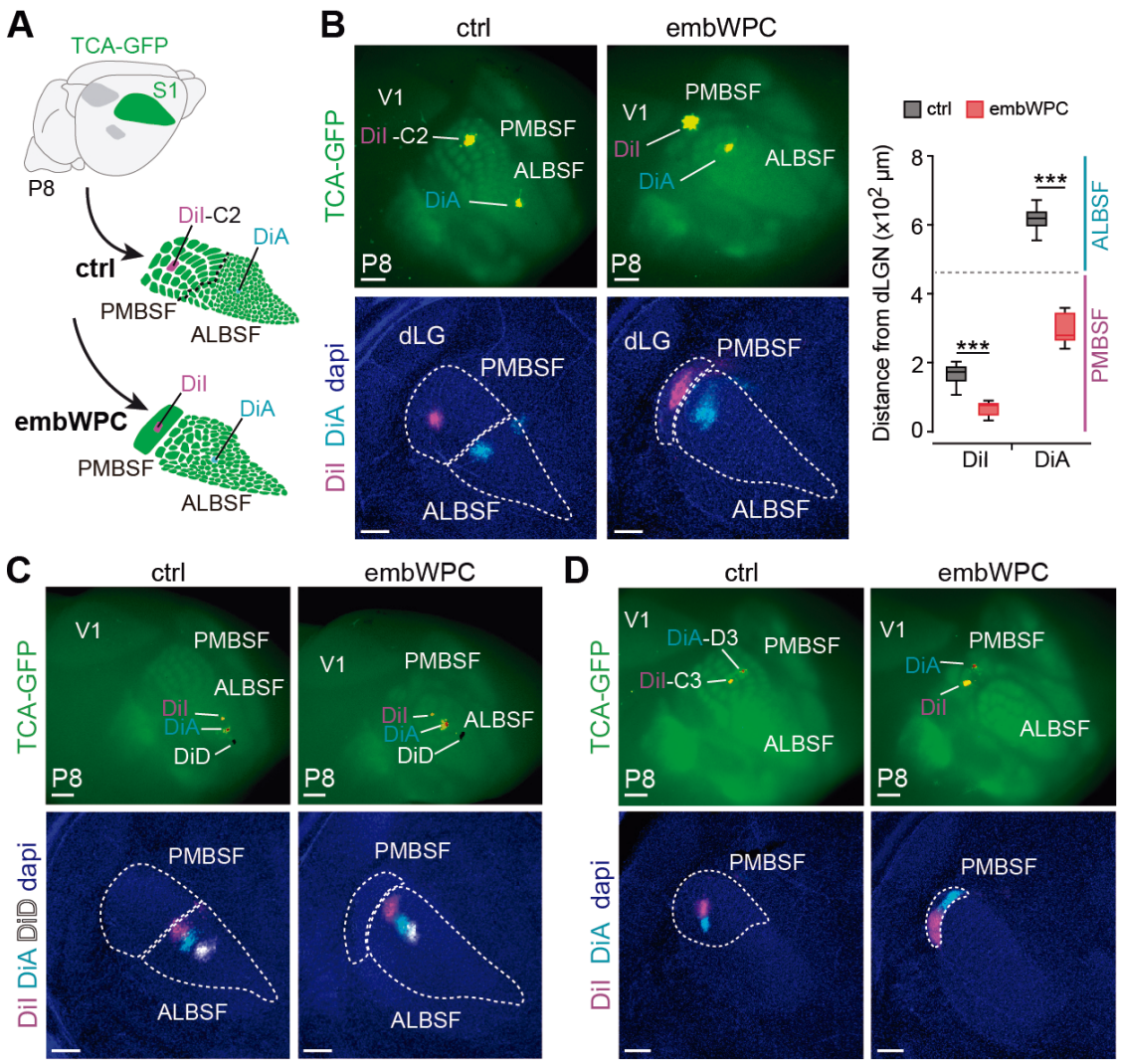

Figure S3. Evaluation of thalamocortical point-to-point topography in embWPC mice, Related to Figures 1 and 2. (A) Schema representing the experimental paradigm. **(B)** Upper panels, DiI and DiA crystal placements in the C2 cortical barrel and in the ALBSF, respectively, in control and embWPC at P8. Lower panels, backlabelled cells at the level of the PMBSF and ALBSF showing the relative displacement of the ALBSF labelling in embWPC mice. Quantification of the position of backlabelled cells with respect to the distance to the dLG nucleus. The gray horizontal dashed line in the graph represents the separation between PMBSF and ALBSF (n= 6 ctrl mice, n= 6 embWPC mice, unpaired two-tailed Student *t*-test). **(C)** Upper panels, DiI, DiA and DiD crystal placements subsequent non-overlapping points in the ALBSF in control and embWPC at P8. Lower panels, backlabelled cells at the ALBSF showed a shifted relative displacement toward the PMBSF in embWPC mice (n= 8 ctrl mice, n= 8 embWPC mice). **(D)** Upper panels, DiI and DiA crystal placements in the C3 and D3 cortical barrels, respectively, in control and in the remaining territory of the PMBSF in embWPC at P8. Lower panels, backlabelled cells maintaining their point-to-point distribution at the PMBSF in control and embWPC mice (n= 9 ctrl mice, n= 9 embWPC mice). dLG, dorsolateral geniculate nucleus; V1, primary visual cortex; DiA, 4-[4-(dihexadecylamino) styryl]-N-methylpyridinium iodide. Scale bars, (top) (B), (C) and (D) 500 µm; (bottom) (B), (C) and (D) 200 µm. Boxplots show the medians with the interquartile range (box) and range (whiskers). ∗∗∗p < 0.001.

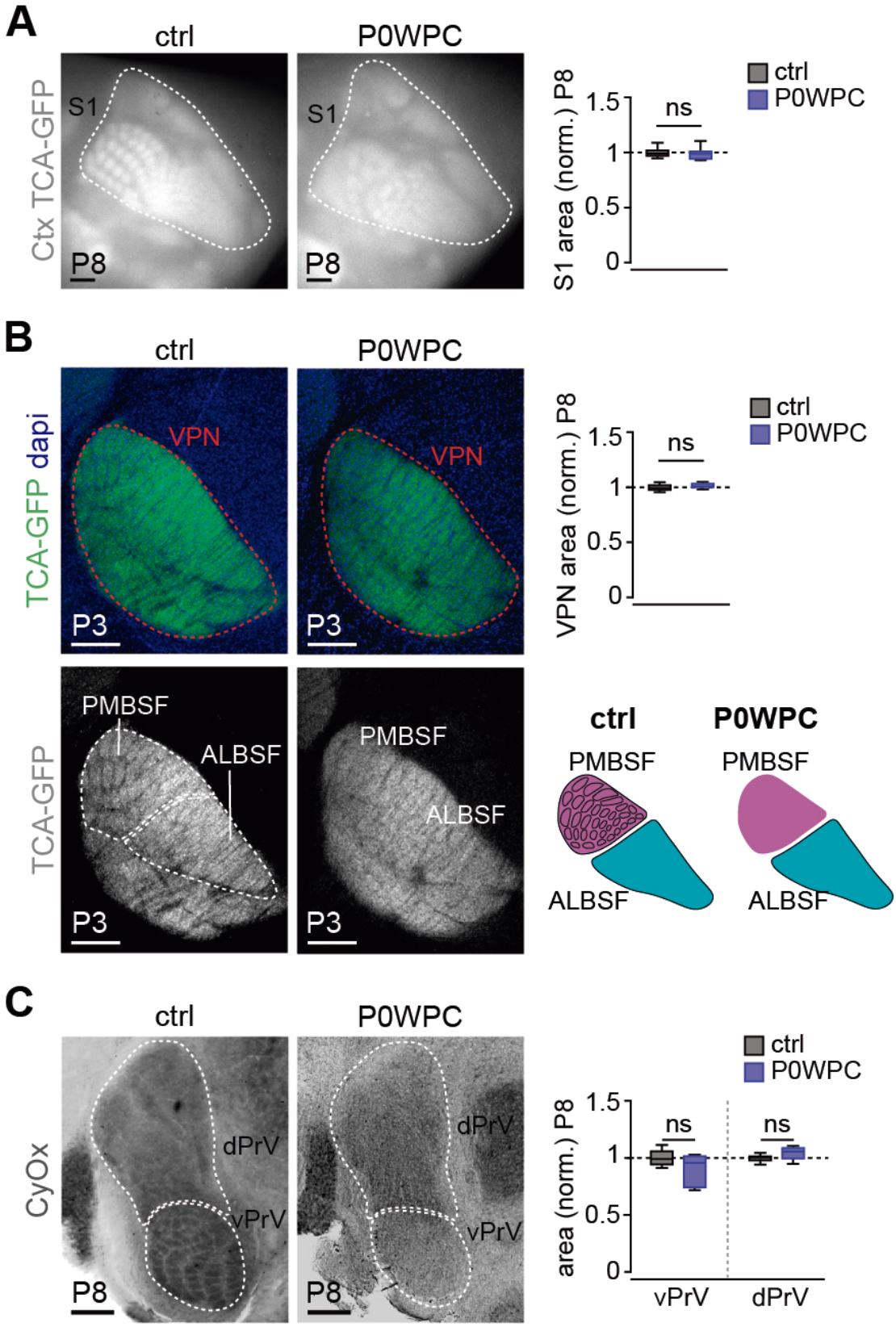

Figure S4. Cortical and subcortical areas for whisker-field representations remained unchanged in P0WPC mice, Related to Figure 1. (A) Surface view of thalamocortical terminals (TCA-GFP+) in the cortical S1 in control and P0WPC mice at P8. Quantification of

the total S1 area (n= 8 ctrl mice, n= 9 P0WPC mice, unpaired two-tailed Student *t*-test. ns, p= 0.66). **(B)** Coronal sections showing TCA-GFP labelling in the PMBSF, ALBSF and VPN of the thalamus in control and P0WPC at P3. Quantification of the VPN area and schema representing the results (n= 8 ctrl mice, n= 9 P0WPC mice, unpaired two-tailed Student *t*-test. ns, p= 0.39). **(C)** Coronal sections of the trigeminal PrV nucleus stained with CyOx in control and P0WPC at P8. Quantification of the vPrV and dPrV area (n= 5 ctrl mice, n= 5 P0WPC mice, unpaired two-tailed Student *t*-test. ns, p> 0.20). P0WPC, postnatal day 0 whisker pad cauterized. Scale bars, (A) 500 μm; (B) and (C) 200 μm. Boxplots show the medians with the interquartile range (box) and range (whiskers). ns, not significant.

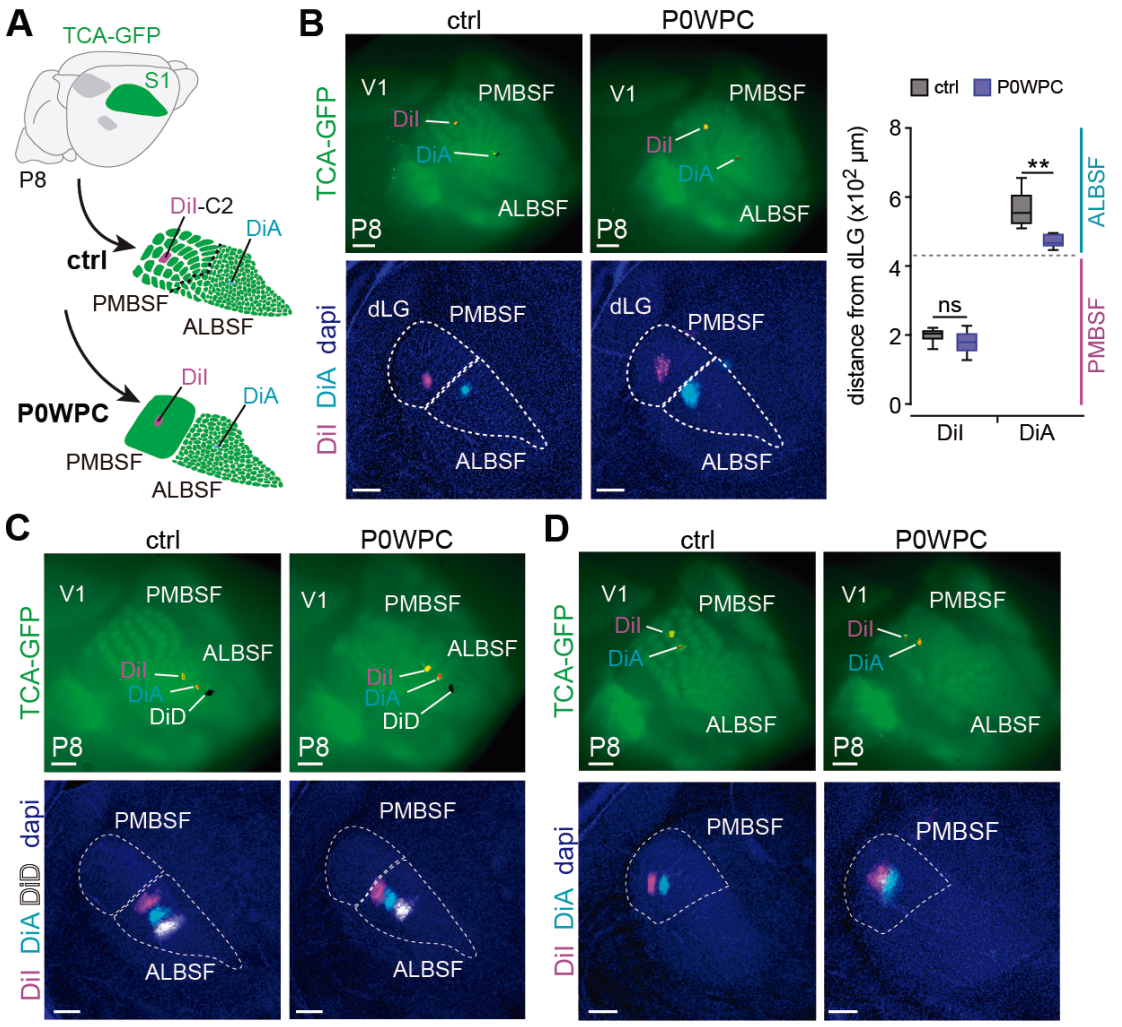

Figure S5. Evaluation of thalamocortical point-to-point topography in P0WPC mice, Related to Figure 1. (A) Schema representing the experimental paradigm. **(B)** Upper panels, DiI and DiA crystal placements in the C2 cortical barrel and in the ALBSF, respectively, in control and P0WPC at P8. Lower panels, backlabelled cells at the level of the PMBSF and ALBSF. Quantification of the position of backlabelled cells with respect to the distance to the dLG nucleus. The gray horizontal dashed line in the graph represents the separation between PMBSF and ALBSF (n= 5 ctrl mice, n= 5 P0WPC mice, unpaired two-tailed Student *t*-test. ns, p= 0.09). **(C)** Upper panels, DiI, DiA and DiD crystal placements subsequent non-overlapping positions in the ALBSF in control and P0WPC at P8. Lower panels, backlabelled cells at the ALBSF (n= 7 ctrl mice, n= 7 P0WPC mice). **(D)** Upper panels, DiI and DiA crystal placements in the C2 and C4 cortical barrels, respectively, in control and in the deprived PMBSF territory in P0WPC at P8. Lower panels, backlabelled cells showing their point-to-point distribution at the PMBSF in control and P0WPC mice (n= 7 ctrl mice, n= 7 P0WPC mice). Scale bars, (top) (B), (C) and (D) 500 µm; (bottom) (B), (C) and (D) 200 µm. Boxplots show the medians with the interquartile range (box) and range (whiskers). ns, not significant. $**p < 0.01$.

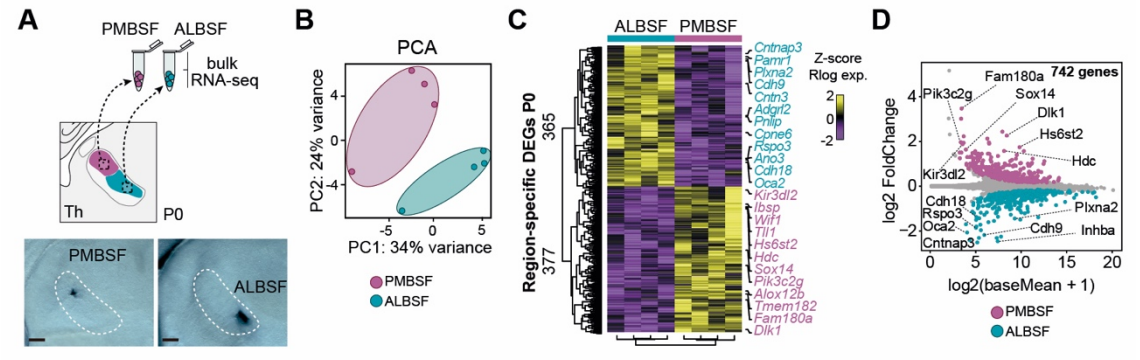

Figure S6. Region-specific transcriptional signatures in the thalamic barrel-representations at P0, Related to Figure 3. (A) Schema representing the experimental paradigm. **(B)** Principal Component Analysis (PCA) of PMBSF (n= 4) and ALBSF (n= 4) control mice at P0. **(C)** Heatmap of normalized regularized logarithm (Rlog) Z-score of expression and unbiased clustering of ALBSF- and PMBSF-specific Differentially Expressed Genes (DEGs) at P0. **(D)** MA plot showing the significance and *P*-value distribution of DEGs. The magenta and cyan dots represent PMBSF and ALBSF DEGs, respectively, with the top 7 protein coding genes listed in every region. Scale bars, 200 μm.

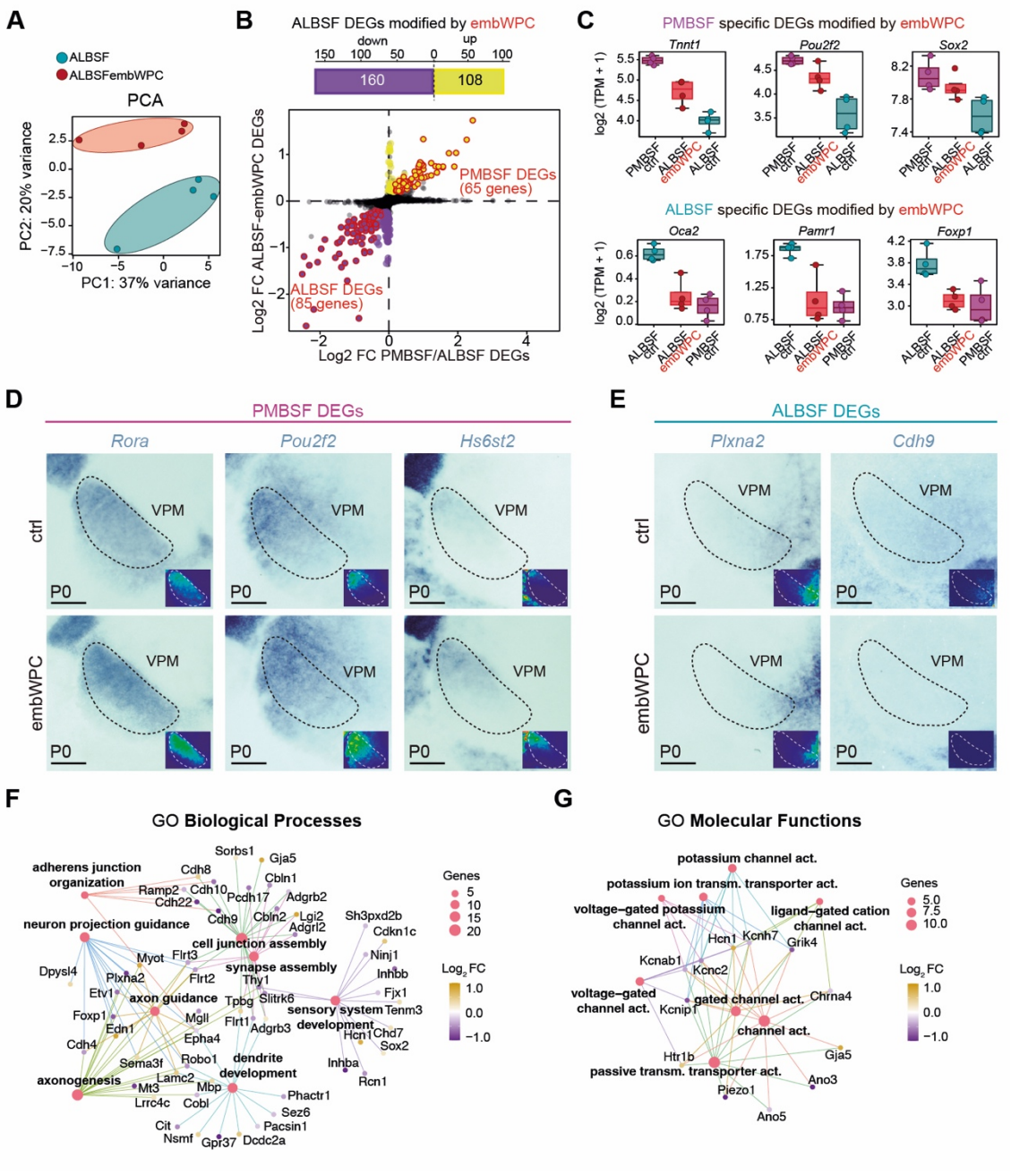

Figure S7. The reorganized ALBSF acquires PMBSF transcriptional signatures, Related to Figure 3. (A) Principal Component Analysis (PCA) of thalamic control ALBSF (n= 4) and embWPC ALBSF (n= 4) mice at P0. **(B)** Upper panel, histogram showing ALBSF Differentially Expressed Genes (DEGs) that are up- and downregulated by embWPC at P0. Lower panel, scatterplot of log2Foldchange between ALBSF DEGs modified by embWPC and PMBSFvsALBSF region-specific DEGs. **(C)** Boxplots showing TPM expression levels of selected PMBSF DEGs and ALBSF DEGs modified by embWPC in the ALBSF. Boxplots show the medians with the interquartile range (box) and range (whiskers). **(D)** Coronal sections showing by in situ hybridization the change in the pattern of expression of PMBSF DEGS in the embWPC mouse at P0 (n= 5 ctrl, n= 5 embWPC, for each probe). **(E)** Coronal sections showing by *in situ* hybridization the change in the pattern of expression of ALBSF DEGS in the embWPC mouse at P0. **(F)** Gene ontology (GO) biological process (BP) enrichment analysis of PMBSF and ALBSF DEGs modified by embWPC in ALBSF. **(G)** Gene ontology (GO) molecular function (MF) enrichment analysis of PMBSF and ALBSF DEGs

modified by embWPC in ALBSF. The size of every node (enriched term) in the gene networks represents the number of genes enriched and the color-code (yellow, high expression; purple, low expression) corresponds to the log2FC in the PMBSF vs ALBSF Differential expression (DE) analysis. VPM, ventroposterior medial nucleus. Scale bars, 200 μm.

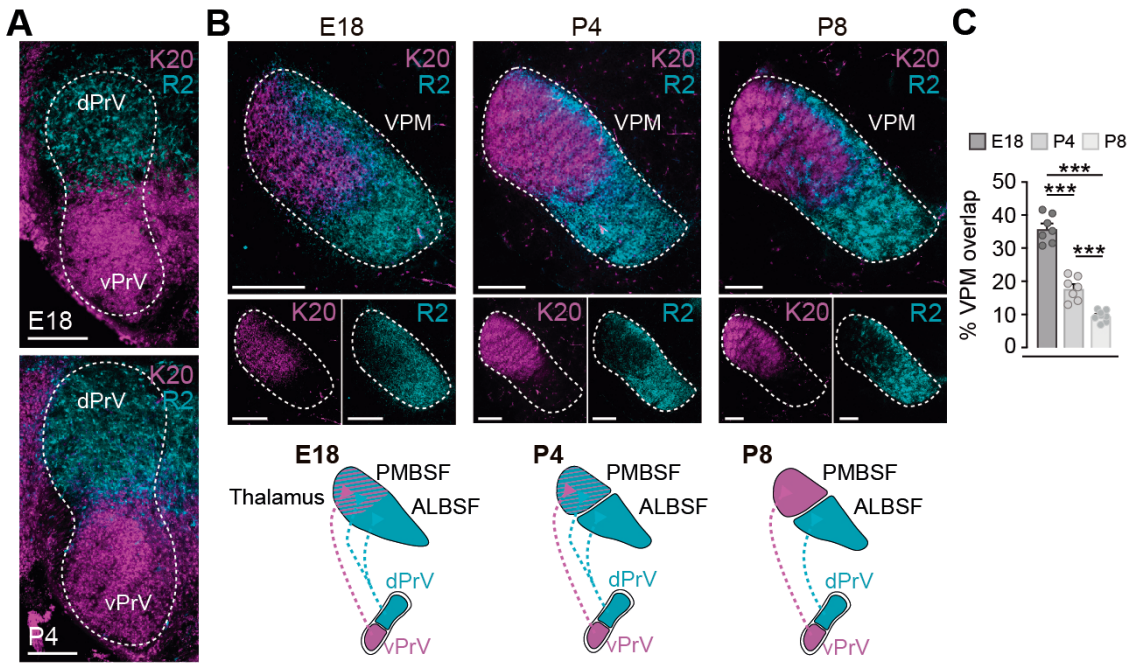

Figure S8. Developmental progression of trigemino-thalamic axons, Related to Figure 4. (A) Coronal sections from the *Krox20-zsgreen::R2-mCherry* double transgenic mouse showing cells expressing Krox20 (magenta) at the vPrV and R2 (cyan) at the dPrV at E18 and P4 (n= 7 E18, n= 7 P4). **(B)** Coronal sections from the *Krox20-zsgreen::R2-mCherry* double transgenic mice showing Krox20-labelled axons (magenta) and R2-labelled axons (cyan) at the VPM of the thalamus at E18, P4 and P8. Schemas representing the results found. **(C)** Quantification of the percentage of developmental overlap of vPrV-dPrV axons at the thalamus (n= 7 E18, n= 7 P4, n= 8 P8, Two-way ANOVA test: ***p <0.001. Tukey's multiple comparison test *post-hoc* analysis). Scale bars, 200 μm**.** Bar graphs show the means ± SEM. ***p <0.001.

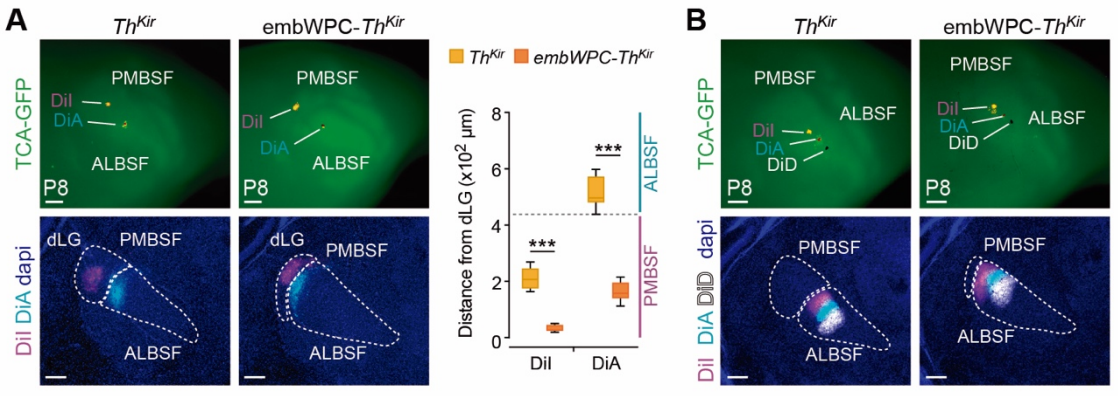

Figure S9. Thalamocortical point-to-point topography is shifted in embWPC-*Th*^{Kir} mice, Related to Figure 4. (A) Upper panels, DiI and DiA crystal placements in the cortical PMBSF and ALBSF areas, respectively. Lower panels, backlabelled cells at the thalamus show shifted positions within the ALBSF thalamic area in the embWPC-*Th*^{Kir} mice as compared to *Th*^{Kir} at P8. Quantification of the position of backlabelled cells with respect to the distance to the dLG nucleus. The gray horizontal dashed line in the graph represents the separation between PMBSF and ALBSF (n= 6 *Th*^{Kir} mice, n= 6 embWPC-*Th*^{Kir} mice, unpaired two-tailed Student *t*-test). **(B)** Upper panels, DiI, DiA and DiD crystal placements in subsequent non-overlapping positions in the cortical ALBSF in *Th*^{Kir} and embWPC-*Th*^{Kir} at P8. Lower panels, backlabelled cells at the ALBSF (n= 6 *Th*^{Kir} mice, n= 4 embWPC-*Th*^{Kir} mice). Scale bars, (top) (A) and (B) 500 µm; (bottom) (A) and (B) 200 µm. Bar graphs show the means ± SEM. ***p <0.001.